UNIVERSITAT POLITÈCNICA DE VALÈNCIA

ESCUELA TÉCNICA SUPERIOR INGENIERÍA INDUSTRIAL VALENCIA

TRABAJO FIN DE GRADO EN INGENIERÍA BIOMÉDICA

STUDY OF OPTOMECHANICAL CAVITIES AS DUAL ULTRA-SENSITIVE BIOSENSORS

AUTHORESS: Ana Sanmartín Senent

SUPERVISOR: Alejandro José Martínez Abietar

SUPERVISOR: Laura Mercadé Morales

Academic year: 2020-21

Acknowledgements

Abstract

Advances in nanotechnology together with an increasing need of ultrasensitive biosensors have drastically raised the interest in the nanoscale fabrication of photonic, nanomechanical and ultimately optomechanical resonators. Cavity optomechanics, which fields the powerful paradigm of light-sound interaction in the nanoscale, emerges as key technology for the highly sensitive detection of biomolecular entities by means of both the optical and mechanical spectra. In this work the sensing potential of a silicon-chip-based ultrahigh frequency optomechanical crystal operating at ambient conditions is demonstrated. The optical and mechanical frequency shifts due to surface functionalization with a monolayer of 3-aminopropyltriethoxysilane (APTES) clearly evidence that optomechanical crystals pave the way towards lab-on-chip label-free bio-sensing for health related applications.

Key words: Biosensing, photonic biosensor, nanomechanical biosensor, optomechanical cavity, optomechanical crystal, frequency shift, functionalization.

Resumen

Los avances en nanotecnología, junto con la creciente necesidad de biosensores ultrasensibles, han aumentado drásticamente el interés por la fabricación a nanoescala de resonadores fotónicos, nanomecánicos y, en última instancia, optomecánicos. La optomecánica de cavidades, que se basa en el poderoso paradigma de la interacción luz-sonido en la nanoescala, emerge como tecnología clave para la detección altamente sensible de entidades biomoleculares por medio de los espectros óptico y mecánico. En este trabajo se demuestra el potencial de detección de un cristal optomecánico de ultra alta frecuencia basado en un chip de silicio que opera en condiciones ambientales. Los cambios de frecuencia ópticos y mecánicos debidos a la funcionalización de la superficie con una monocapa de 3-aminopropiltrietoxisilano (APTES) evidencian claramente que los cristales optomecánicos allanan el camino hacia la biodetección lab-on-chip sin etiquetas para aplicaciones relacionadas con la salud.

Palabras clave: Biosensado, biosensor fotónico, biosensor nanomecánico, cavidad optomecánica, cristal optomecánico, cambio en frecuencia, funcionalización.

Resum

Els avanços en nanotecnologia, juntament amb la creixent necessitat de biosensors ultrasensibles, han augmentat dràsticament l'interés per la fabricació a nanoescala de ressonadors fotònics, nanomecànics i, en última instància, optomecànics. L'optomecànica de cavitats, que es basa en el poderós paradigma de la interacció llum-so en la nanoescala, emergeix com a tecnologia clau per a la detecció altament sensible d'entitats biomoleculars per mitjà dels espectres òptic i mecànic. En aquest treball es demostra el potencial de detecció d'un cristall optomecànic d'ultra alta freqüència basat en un xip de silici que opera en condicions ambientals. Els canvis de freqüència òptics i mecànics deguts a la funcionalizació de la superfície amb una monocapa de 3-aminopropiltrietoxisilano (APTES) evidencien clarament que els cristalls optomecànics aplanen el camí cap a la biodetecció lab-on-chip sense etiquetes per a aplicacions relacionades amb la salut.

Paraules clau: Biosensat, biosensor fotònic, biosensor nanomecánico, cavitat optomecánica, cristall

optomecánico, canvi en freqüència, funcionalizació.

Contents

Part I

Memory

Chapter 1

INTRODUCTION

1.1 Motivation

Sensing applications for medical diagnostics rely on sensitive detection to examine external physical parameters [1]. The increasing need for rapid, ultrasensitive, and economical methods for the detection of biochemical entities, such as virus particles, proteins or cancer biomakers, has boosted the development of biosensors. Biosensors are used for the detection of target molecules because they are capable of measuring the physicochemical changes that a biological recognition layer adhered to a solid transducer undergoes when it interacts with the molecule desired to be detected [2].

Particularly, the nanoscale fabrication of highly sensitive nanomechanical lab-on-a-chip sensors emerges as key technology [3], given that the advances in nanofabrication technologies enable the preparation of ever-smaller mechanical transducers [2], which can be used to measure mass changes. Note that the minimum detectable mass is proportional to the effective mass of the oscillator [4]. In fact, nanomechanical resonators have already proved their capability of sensing individual atoms in vacuum conditions [4].

Simultaneously, optomechanical (OM) cavities have arised as promising platforms for precision sensing [5]. Cavity optomechanics, that adresses a light-matter interaction phenomena, enables the manipulation of mechanical motion through optical fields tightly confined in deformable cavities [6]. Consequently, any perturbation to the cavity resonance wavelength, $\delta\lambda$, is reflected on a frequency shift of the mechanical motion, δf_m [1].

The purpose of this work is to demonstrate how OM crystal cavities can serve as dual-ultra sensitive biosensors. An optomechanical crystal cavity is an OM device that has been enginereed in order to confine optical and mechanical modes by means of the design of both a photonic and a phononic crystal cavity into the same structure. Therefore, the aim is to display their sensing potential by detecting the presence of surface biofunctionalization through both an optical and mechanical frequency shift from the original cavity response, as can be seen in Figure 1.1. Here, a tunable laser is fed into a cavity and then its optical and mechanical response is photodetected and analyzed before an after surface functionalization.
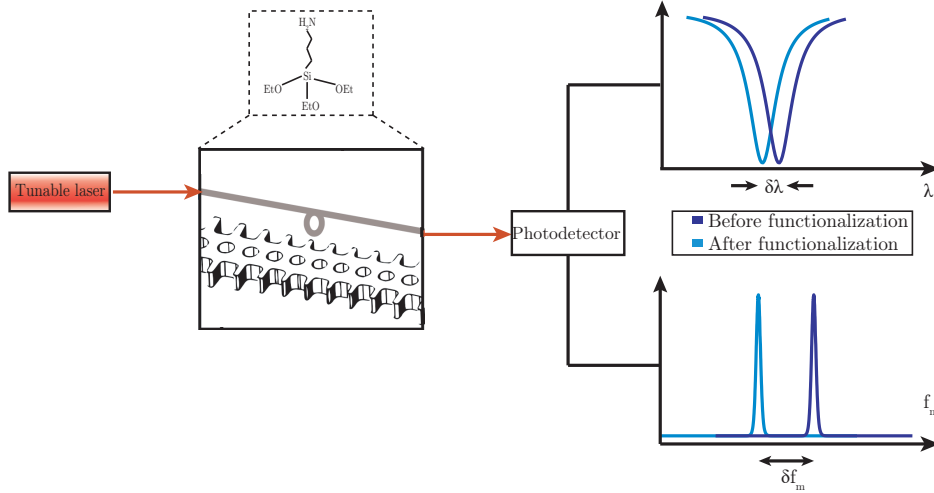
Figure 1.1: General scheme depicting the expected optical and mechanical frequency shift due to biofunctionalization. The experimental setup used to obtain the optical and mechanical spectra will be fully detailed in Section 3.2.1.

1.2 Justification

The minimum resolvable frequency shifts determine mass resolution [7]. The relation between mass changes in an oscillator (Δm) and mechanical frequency shifts (Δf) is given by Equation 1.1 [8], where f_0 is the resonant frequency and m_{eff} is the effective mass. The theoretical minimum detectable mass of the OM crystal presented in this work is $\Delta m_{min} = 2.7*10^{-23}$ kg, according to Equation 1.1 and given that $f_0 = 3.897$ GHz, $m_{eff} = 2.7*10^{-16}$ kg and $\Delta f_{min} = 195$ Hz (frequency fluctuations are characterized by the Allan deviation) [6, 9]. Note that Equation 1.1 assumes that the adsorbed mass is uniformly distributed throughout the cavity.

$$\Delta m = -\frac{2*m_{eff}}{f_0}*\Delta f \tag{1.1}$$

The fact that our system can theoretically resolve masses as low as 10^{-20} g, together with the added possibility of detecting the presence of a substance with a different index of refraction through an optical resonance shift, clearly justifies the need of studying OM crystals as dual ultra-sensitive biosensors. Note that according to Bar-on et al. [10], a single virus particle of SARS-CoV-2 (COVID-19) weighs 1 fg, that is 10^{-15}g.

1.3 Objectives

The objective of this work is to experimentally demonstrate that an OM cavity built on a silicon chip performs simultaneously as a refractive index photonic sensor and a nanomechanical mass sensor, in both cases being able to detect molecular layers attached to its surface. It must be noted that no target analyte will be detected in this work, but by proving the biosensor's capability of detecting an attached layer to its surface, the OM cavitiy capability of detecting molecules that selectively bind to the biofunctionalized surface is demonstrated.

1.4 Methodology and working plan

In order to demonstrate the performance of the OM crystal cavity as a dual biosensor, an experimental characterization of the working devices as well as a functionalization of the samples under study has been performed. The experimental data has been acquired by means of the optomechanical setup described in Section 3.2.1. The optomechanical characterization setup and the setup used in the functionalization procedure can be found in the laboratories at the Nanophotonics Technology Center, where all the experiments were conducted.

To analyse the experimental data both the Data Analysis and Graphing Software OriginLab [11] and the Programming and Numeric Computing Platform Matlab [12] have been used. Adobe Illustrator has been utilized to edit graphs and figures.

The project schedule depicting the average time spent on each task is shown in Figure 1.2.
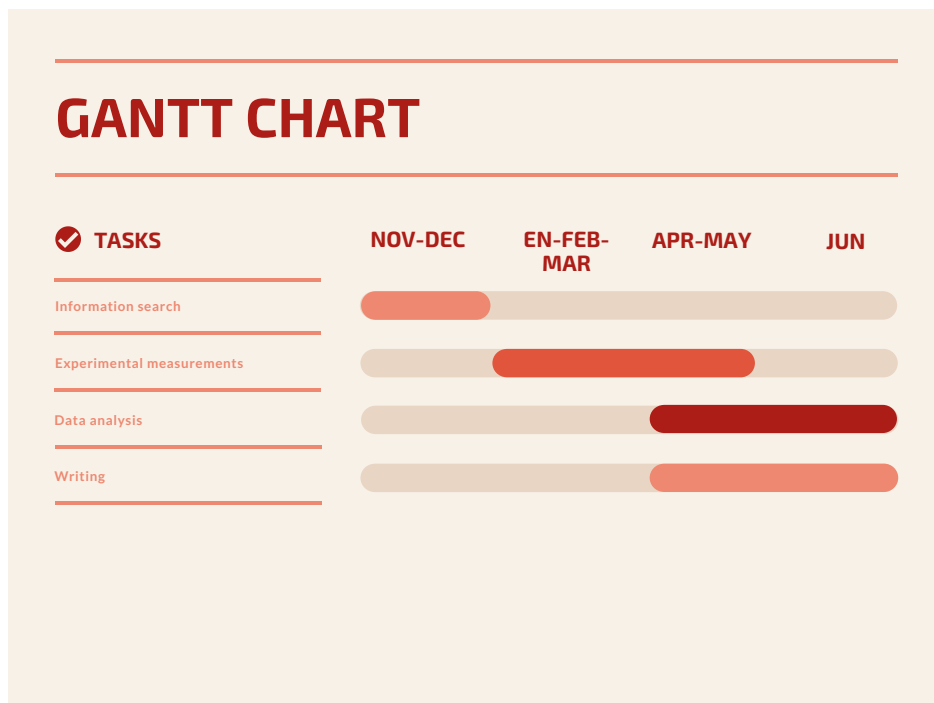

Figure 1.2: Project schedule.

Chapter 2

THEORETICAL STUDY

2.1 Photonic biosensors

Photonic biosensors are widely used for performing sensitive and label free detection of biomolecular entities. Even though multiple architectures have been developed (such as surface plasma resonance (SPR) sensors [13] and whispering gallery modes sensors [14]), nearly all of them rely on the same detection principle: a change in the refractive index (for example due to an added mass) translates in a change in the wavelength of the resonant peak [15].

The Nanoscale Optofluidic Sensor Arrays (NOSAs) proposed by Mandal et al. [15] will be described because their optical sensing architecture is based on planar photonic crystal (PhC) sensors like in the OM crystal cavities presented in this work. Their sensor design consists of a silicon waveguide with a series of evanescently coupled side resonators (Figure 2.1(a)). This side resonators are 1D PhC micro-cavities formed by a central defect cavity and 8 holes [15]. When light transmitted through the waveguide corresponds to the resonant wavelength of the resonator a dip in the output spectrum of the waveguide can be observed [15]. By placing a large number of side resonators with different resonant wavelength along one same waveguide one can be able to perform many detections in parallel. They demonstrated that their device is capable of incorporating up to 50 sides resonators, thus, of performing 50 parallel detections. To this end, they placed five side resonators along a single waveguide and targeted one of them with a fluidic channel at first filled with water. When Calcium Chloride (higher refractive index in comparison to water) was injected, its unique resonant dip experienced a redshift (increase in wavelength) whilst the peaks corresponding to the other resonators remained unchanged (Figure 2.1(b)).

2.2 Nanomechanical biosensors

Nanomechanical resonators perform as precision mass sensors due to the fact that their resonant frequency, which is related to their mass, shifts when a particle adsorbs to the resonator and notably increases the resonator's effective mass [8]. Multiple nanomechanical mass sensors have been demonstrated based on monitoring the bending induced by the added mass (quasistatic mode), or the shift of the mechanical resonant frequency (dynamic mode) [16].
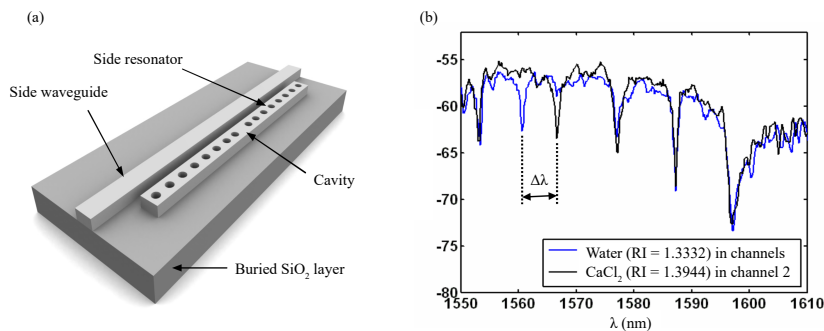
Figure 2.1: (a) Illustration of the sensor design. (b) Output spectrum before and after injection of CaCl$_2$. Source: [15].

Surface-stress mechanical biosensors measure the quasistatic deflection of a miniature device due to the binding of target analytes to the functionalized surface of the device [17]. The most common architecture is a cantilever as that proposed by Fritz et al. [18]. In their study they demonstrated how microfabricated cantilevers were capable of detecting a single DNA base mismatch by a nanomechanical response. They achieved this by inmobilizing a monolayer of receptor molecules on one side of the cantilevers differing in only one base and detecting the nanomechanical bending of the cantilevers after injection of the complementary oligonucleotides in a liquid environment (Figure 2.2) [18].
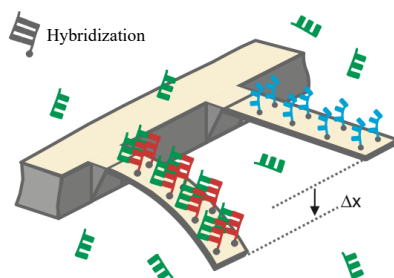

Figure 2.2: Illustration of the differential deflection of the cantilevers depending on the binding of the molecules. Source: [18].

Dynamic-mode mechanical biosensors oscillate with a resonance frequency that changes when depositing an added mass [17]. Examples of nanomechanical resonators operating in dynamic-mode include carbon-nanotubes [8, 19], cantilevers [3], suspended microchannels [20] and NEMS (nano-electromechanical mass sensors) [7].

Chaste et al. [19] have evidenced the ultra-sensitivity of nanotube resonators by detecting the adsorption of a xenon atom and of C$_{10}$H$_8$ molecules on the nanotube surface because of decreased resonance frequency, obtaining a resolution as low as 1.7 yoctograms. However, this requires ultrahigh vacuum conditions and liquid-helium temperature. Vacuum and cryogenic conditions generate limitations for practical applications.

Gupta et al. [3] were able to detect a single virus particle by means of a silicon cantilever. The frequency spectra of the cantilever beam was measured before and after loading the virus particle (Figure 2.3(a)). The resonant frequency of the cantilever decreased by 60 kHz after the addition of the single virus particle of mass 9.5 fg, as shown in Figure 2.3(b).

Burg et al. [20] observed real-time antibody-antigen binding by monitoring the resonance frequency
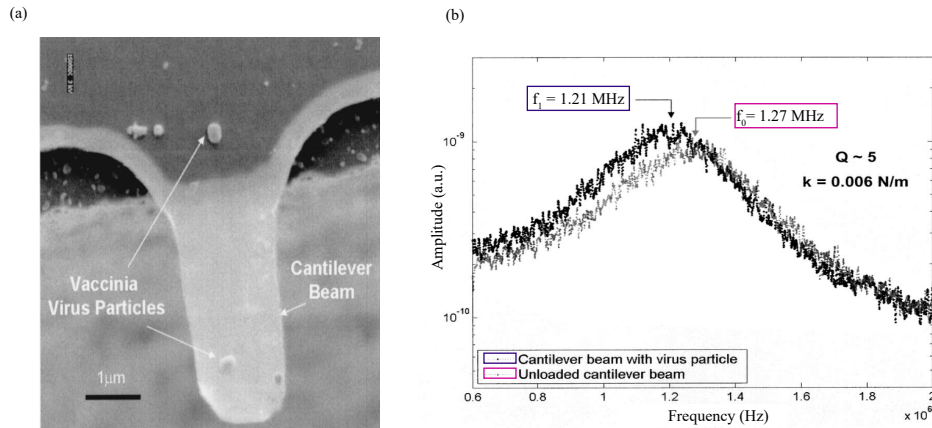
Figure 2.3: (a) SEM image showing a cantilever beam with a single *Vaccinia* virus particle. (b) Frequency shift due to the deposition of the virus particle. Source: [3].

of suspended microfluidic channels because changes in mass inside the channel translate into shifts in the resonance frequency (Figure 2.4). To this end, anti-mouse IgG antibodies were inmobilizied on the channel walls and different concentrations of anti-mouse IgG were injected. Additionally, they were able of weighing individual live bacteria of *Escherichia coli* and *Bacillus sutilis* bacterial cultures.
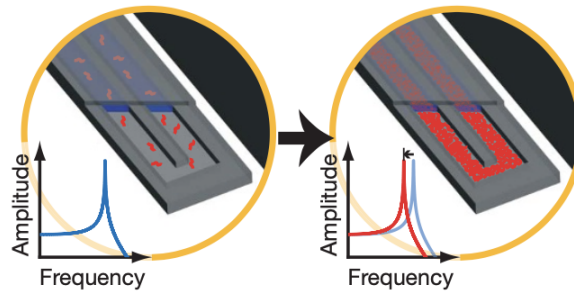
Figure 2.4: Illustration of the frequency shift due to bound molecules to the channel wall. Source: [20].

Hanay et al. [7] used a multimode NEMS-based device to determine the mass of individual IgM antibody complexes and individual 5 nm and 10 nm gold nanoparticles adsorbed to the resonator in real-time. It is possible to fulfill mass measurements from the frequency shift by using information from multiple modes, so they studied real-time frequency jumps of two mechanical modes.

Table 2.1 compiles the main characteristics of the resonators presented in these studies. Notice that for mainstream applications, it would be highly desirable to have ultra-sensitive mass sensors (ultimately being able to detect single molecules) operating at room temperature and ambient conditions.

2.3 Optomechanical cavities

2.3.1 Cavity optomechanics: coupling light and sound at the nanoscale

Cavity optomechanics fields the interaction between light and sound confined in a cavity [6, 21, 22]. To understand the concepts underlying optomechanical (OM) cavities one can consider the Fabry-

Pérot resonator, which is the canonical form of an optical cavity with deformable boundaries. The functioning of a Fabry-Pérot cavity is based on two highly reflective mirrors, one of them being movable due to its connection to a spring (Figure 2.5). When a photon beam is injected to the cavity using a laser, light will be confined at a certain wavelength on account of the aforementioned mirrors. The confined wavelength or frequency depends on the distance between these two mirrors, L in Figure 2.5. Moreover, the fact that one of them is movable enables the confined photons to produce the displacement of the mirror through a phenomen known as radiation pressure.
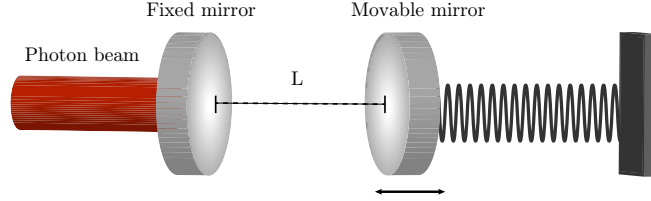

Figure 2.5: Shematic diagram of a Fabry-Pérot cavity

Radiation pressure coupling that occurs in a Fabry-Pérot cavity is described as the momentum transfer of photons due to reflection, given by equation 2.1, where $| \Delta p|$ is the momentum transfer of a single photon, h is Plank's constant and λ is the photon wavelength [22].

$$|\Delta p| = \frac{2 * h}{\lambda} \qquad (2.1)$$

Mechanical modes are therefore activated through the radiation pressure forces exerted by the confined photons. The displacement of the movable mirror will in turn produce a frequency change of the optical mode, because of the adjustment of L. Otherwise stated, the optical wave cycling inside the microcavity is able to produce a radiation pressure that interacts with the mechanical motion of the device [1], giving rise to optomechanical coupling. The interaction strength between optical and mechanical resonances is given by the OM coupling rate, g_0 [6]. In general, a high OM coupling rate requires highly localized and overlapped optical and mechanical fields.

With a high optical quality factor Q_o, the laser light inside the cavity leads to a strong radiation pressure [5]. Therefore, there is a strong coupling between the optical and mechanical modes in a high-Q_o oscillator because of the radiation pressure exercised by the large circulating optical power [16]. Q_o measures the goodness of the system as a resonator, because it measures the ratio of photons that remain oscillating in the cavity to those that are disipated, according to Equation 2.2. Low losses are required to obtain a high Q.

$$Quality\ Factor\ Q = 2\pi * \frac{stored\ energy}{energy\ lost\ per\ cycle} \qquad (2.2)$$

OM cavities range from microtoroids [16] and microspheres [1] to OM crystal cavities [6, 23], which is the type of cavity used in this work. Therefore, OM cavities span an enormous range of effective masses (from g to zg) and mechanical eigenfrequencies (from Hz to hundres of GHz). However, an astonishing fact about this field is that, even though those objects are completely different, they can be described by roughly the same formalism used for the Fabry-Pérot cavity of Figure 2.5.

2.3.2 Optomechanical crystal cavities

The underlying idea behind OM crystal cavities is to build periodic lattices that alter simultaneously the flow of photons and phonons. Therefore, OM crystals act both as photonic and phononic crystal [23, 24], reason why some authors refer to them as phoxonic crystals [25]. Photonic crystals (PhCs) are engineered by applying periodicity to the refractive index of a material, tightly confining light resonantly [24]. Likewise, phononic crystals apply periodicity in the acoustic impedance of a certain propagating medium generating energy intervals for which mechanical modes cannot propagate inside the medium [26]. Hence, OM crystals are periodic structures that exhibit forbidden bandgaps for both electromagnetic and elastic waves [25, 26].

OM crystal cavities were demonstrated for the first time in a study by Eichenfield et al. [24] in 2009. Figure 2.6(a) and (b) show a SEM image of the OM crystals presented in their work, which are similar to the ones used in this project. The optical spectra of the nanobeams is shown in Figure 2.6, depicting how their cavity had three optical modes. Furthermore, the mechanical spectra is displayed in Figure 2.6(c)-(g). It can be appreciated that their cavity presented, from the lowest to the highest frequency, the following mechanical modes: ~200 MHz (corresponding to compression modes of the entire beam), 850 MHz (the so-called pinch modes), 1.41 GHz (accordion modes) and 2.25 GHz (breathing modes) [24]. On top of that, they were the first to observe the phonon lasing phenomen (Figure 2.6(h)), which will be explained in Section 4.2.2.
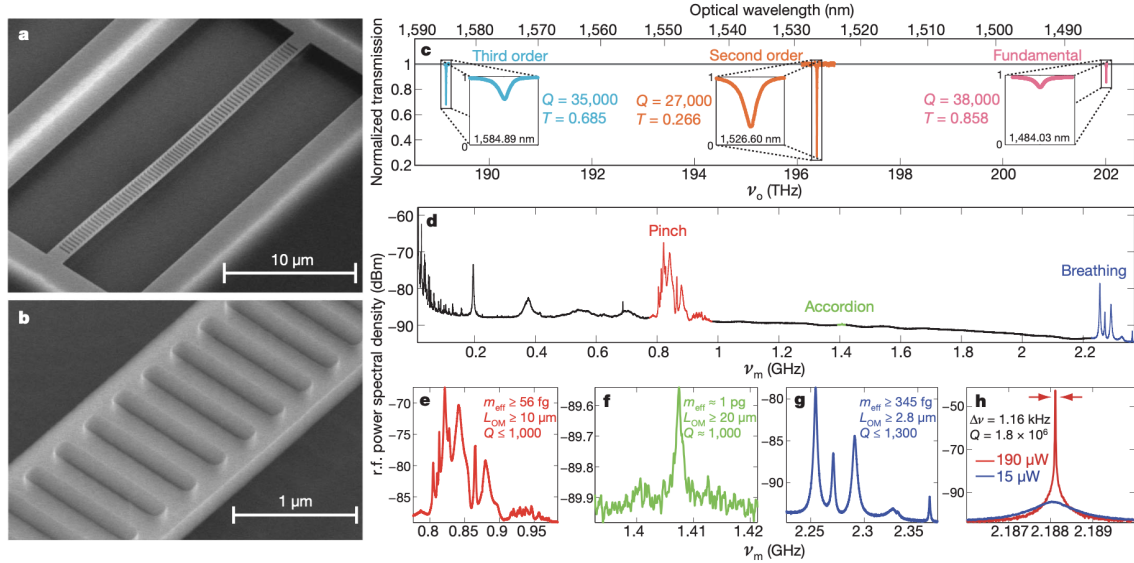

Figure 2.6: (a),(b) SEM images of the fabricated OM crystals in a silicon nanobeam. (c) Optical spectra. (d)-(g) Mechanical spectra. (h) Phonon lasing. Source: [24].

The OM crystals used in this work are OM cavities lithographically defined on suspended layers of high-index silicon nanobeams with 1D periodicity [6] as illustrated in Figure 2.7. To allocate confined modes in the OM cavity center, a defect is created in the center of the nanobeam and the main parameters (such as the holes size) are adiabatically changed towards the ends [6]. The cavity's unit cells are engineered in order to have an OM mirror that exhibits a TE-like photonic bandgap and a full phononic bandgap [6]. Lateral corrugations in addition to the holes are required in order to achieve a full phononic bandgap [6]. The optical and mechanical modes positioned in the bandgaps can propagate in the defect cell but not in the OM mirror unit cells and are therefore tightly confined in the cavity center [27]. The fabricated structures present different mechanical and optical modes from the theoretical ones due to fabrication imperfections [6], so the OM cavities have been experimentally characterized in this work.

The optical and mechanical field displacements in the central region of the cavity are shown in Figure 2.8. These COMSOL simulations show how the electromagnetic and mechanical fields are confined in the same region, resulting in a g_0 of approximately 540 KHz, in accordance with the state of the art.
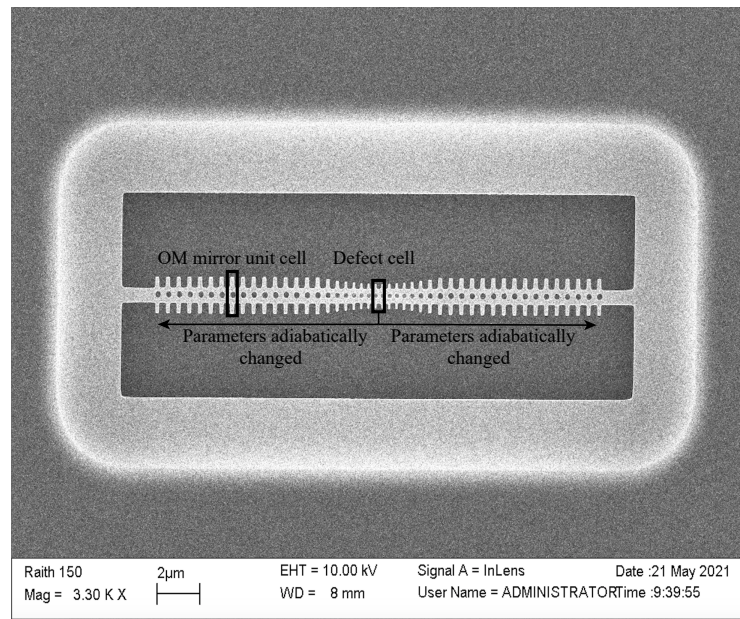

Figure 2.7: OM crystal cavity structure. Optical and mechanical modes are confined around the defect cell.
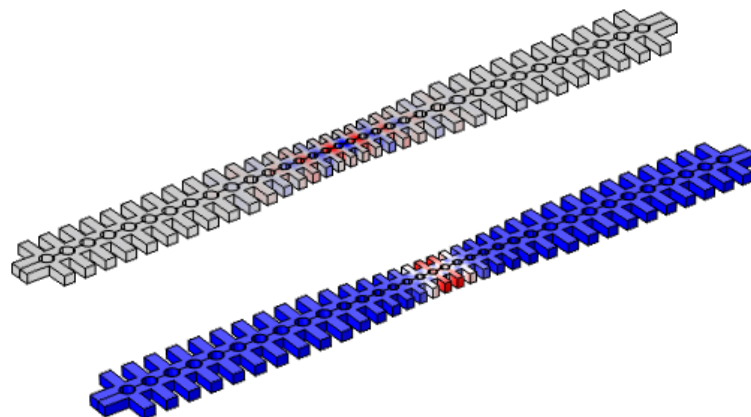

Figure 2.8: Optical and mechanical field displacement obtained through the COMSOL simulation of the designed structure.

2.4 Optomechanical cavities as dual biosensors

Sensing sensitivity is enhanced by reducing the resonator dimension and mass and by increasing the fundamental mechanical frequency [3, 4, 16, 17, 20]. This is apparent from Equation 1.1, where the shift in resonant frequency Δf is maximized when reducing the mass of the resonator m_0 while maintaining high resonance frequencies f_0 [8]. Note that until 2003, when Hengry Huang et al. [28] achieved a NEMS with eigenfrequencies at 1.014 GHz and 1.029 GHz, nanodevices operating with fundamental frequencies beyond 1 GHz were inaccesible.

In a study by Liu et al. [16], they demonstrated the use of a large silica microtoroid as an optome-chanical oscillator (OMO). To this end, the optical driving power was provided by a near-IR tunable laser that coupled into and out of the microtoroid cavity using a silica fiber taper [16]. They studied the mass sensing potential on two distinct mechanical modes excited on two different microtoroids by monitoring the optically generated harmonics before and after depositing the added mass. Concretely, they sequentially placed polyethylene microspheres with diameters ranging from 0.5 μm to 0.2 μm and masses between 0.1 and 4 pg on the silica microtoroids [16]. The decrease in the fundamental optomechanical oscillation frequency and its harmonics suggest that the OMO microtoroid can be applied as a sensor. However, the microtoroids presented a major diameter of D = 131 μm and D = 133 μm (Figure 2.9), and a fundamental optomechanical oscillation frequency of f_{OMO} = 8.505 MHz and f_{OMO} = 24.88 MHz, respectively. Therefore, this OMO is useful for applications where ultra-low sensitivity is not required [16].
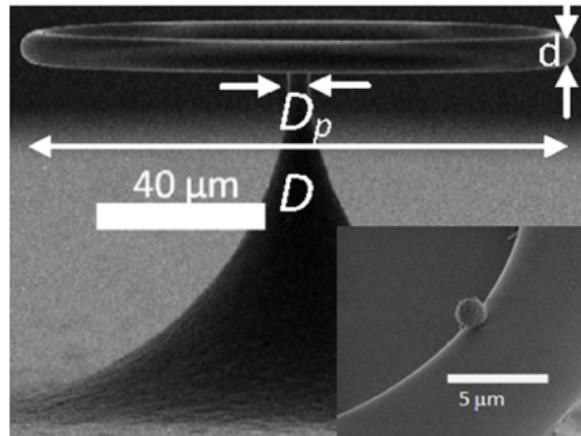
Figure 2.9: SEM image of the silica microtoroid. Source: [16].

Navarro-Urios et al. [23] recently proposed a silicon OM crystal cavity as a novel sensor. They compared the mechanical spectrum before and after placing one and two particles of diameter 495 nm. However, the cavity is designed in order to support low modal-volume mechanical modes (pinch modes) [23]. Therefore, the eigenfrequencies of the mechanical modes are on the order of MHz. Concretely, they measured frequency shifts corresponding to RF peaks from 480 MHz to 550 MHz. Additionally, the optical spectra did not change significantly.

Vibration modes of biological particles, such as proteins, viruses and bacteria, carry information on their structure and mechanical properties, so these characteristic vibrational frequencies can be used as a fingerprint to identify this bioparticles [29, 30]. Gil-Santos et al. [29], by means of a high frequency OM disk resonator, were able to measure the vibration mode of a single bacteria entity. To this end, they deposited a single *S. epidermidis bacterium*, of radius 400 nm, on two different OM disks (Figure 2.10). These disks were of radius 5 μm and 2.5 μm, and exhibited fundamental frequencies of 272 MHz and 546 MHz, respectively. When depositing the bacterium in the larger disk, the resonance frequency

decreased because of the added mass. However, they found out than when depositing the bacterium in the smaller disk, the resonance frequency splited into two wide and close resonances. This phenomen of frequency splitting is observed when nearly identical resonators are coupled [29]. They ascertained that the bacterium presented a resonance frequency of 541 MHz. Note that bacterium are smaller entities than virus and therefore exhibit lower vibrational modes.
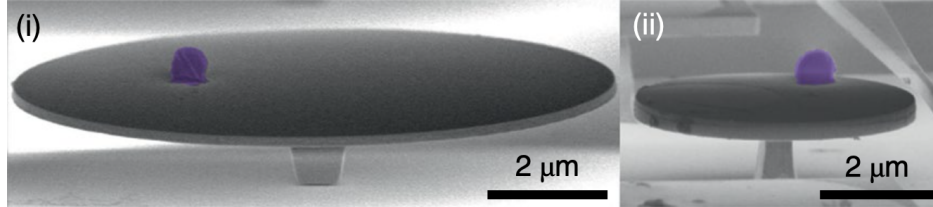

Figure 2.10: SEM image of the two optomechanical disk resonators with an attached S. epidermidis cell. Source: [29].

Viruses are of nanometer size scale and, thus, predicted to exhibit fundamental frequencies in the GHz frequency range [30]. Burkhartsmeyer et al. [30] found that the vibrational frequency of a *PhiX174* virus, sized 25 nm, was 32 GHz. As concluded by Gil-Santos et al. [29], in order to fingerprint biological particles by their vibrational properties the device eigenfrequencies must be close to the vibration frequencies of the analyte. In this work, the sensing potential of an OM crystal cavity operating at room temperature, that has an ultrahigh frequency breathing-like mechanical mode at approximately 3.897 GHz [6] is demonstrated. The biosensor presented in this project could be able to detect virus particles because it exhibits higher eigenfrequencies than that proposed by Gil-Santos et al. [29].

Table 2.1 summarizes the main characteristics of the nanomechanical and optomechanical sensors described in this chapter. Here, 1 yg $=10^{-24}$g, 1 fg $=10^{-15}$g, 1 ag $=10^{-18}$g, 1 MDa = 1,66054*10^{-18}g and 1 kDa $=1.66054*10^{-21}$g. TLD stands for theoretical limit of detection. The box marked with an asterisk (*) is due to the fact that the demonstrated detection is the purpose of this work and will be disclosed in Section 5.1.

OM crystals are promising sensing platforms because they provide a combination of the sensing characteristics of PhCs and NEMS [23]. The fact that OM cavities are also photonic cavities enables one to take advantage of the changes in the optical resonance due to the deposition of a mass with different refractive index to have a photonic sensor. Therefore, OM crystals lead to the detection of a substance by means of both the optical and mechanical spectra. Note that if the deposited mass has the same refractive index, the OM crystal would only undergo a mechanical frequency shift and vice versa.

Table 2.1: State-of-the-art nanomechanical sensors.

Reference	Resonator	Resonant frequency	TLD	Demonstrated detection	Operation conditions	Excitation/Readout
[19]	Carbon nanotube	1.86 GHz	yg	Xenon atom 10^{-22}g	Vacuum and cryogenic conditions	Electrical/Electrical
[3]	Cantilever	1.27 MHz	-	Virus particle fg	Ambient conditions	Optical/Optical
[20]	Suspended microchannel	220.5 kHz	ag	Single bacteria fg	Vacuum	Electrical/Optical
[7]	NEMS	44.6 MHz	kDa	Human IgM MDa	Vacuum and cryogenic conditions	Electrical/Electrical
[16]	OM microtoroid	24.88 MHz	fg	Polytethylene microspheres pg	Ambient conditions	Optical/Optical
[23]	OM crystals	480-550 MHz	-	Submicrometer sized particle (10^{-13}g)	Ambient conditions	Optical/Optical
[29]	OM disk resonator	546 MHz	-	Single bacteria	Ambient conditions	Optical/Optical
This work	OM crystal	3.897 GHz	10^{-20}g	*	Ambient conditions	Optical/Optical

Chapter 3

EXPERIMENTAL CHARACTERIZATION

3.1   Functionalization of optomechanical cavities using APTES

To demonstrate the performance of the OM cavities under study as a dual biosensor, a surface functionalization on the sample will be performed. Concerning this, surface functionalization is the process of chemical deposition on the surface to provide selectivity in molecular detection. Therefore, biofunctionalization is necessary because it enables the detection of the target analyte. The molecule used to biofunctionalize is the organosilane 3-aminopropyltriethoxysilane, commonly known as APTES. As a coupling agent, APTES has the ability to form a durable bond between organic and inorganic materials [31]. This alkoxysilane is frequently chosen because the terminal amine group allows further functionalization [32]. It should be noted too that the amino group can be protonated with HCl, becoming positively charged, and therefore being able to link with a negatively charged molecule.
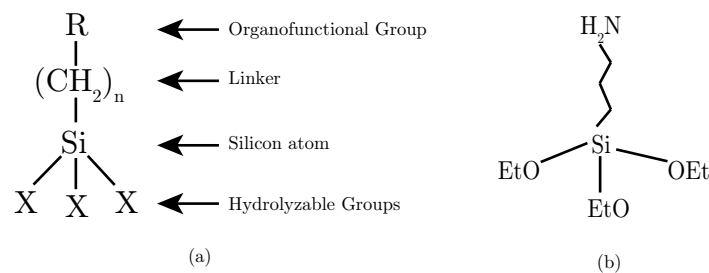
Figure 3.1: (a) General chemical structure of a trialkoxysilane. (b) Chemical structure of APTES.

3.1.1   Sample preparation

In order to achieve the biofunctionalization, the silicon wafers must be firstly hydroxylated. Hydroxilation is the chemical oxidation process that gives rise to a silicon dioxide layer with hydroxyl groups (-OH), as shown in Figure 3.2. This functional group is needed to ensure that silanization, the process used to attach APTES to the surface, will satisfactorily take place [32, 33]. Moreover, this first phase also cleans the samples which is necessary too.

In that regard, two different methods for the creation of the -OH groups were explored; either using oxygen plasma or the $NH_3/H_2O_2/H_2O$ sonicating technique. Two different samples were studied for each technique. This was made in order to prevent breakage of the samples where the characterization of the optomechanical response before and after the functionalization was going to be performed. Therefore, a different set of samples with suspended optomechanical cavities for each procedure was used.
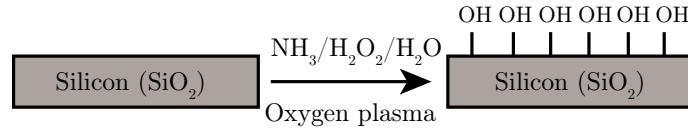

Figure 3.2: Hydroxylation of silicon giving rise to a hydroxylated surface.

$NH_3/H_2O_2/H_2O$ sonicating technique

The first attempt was working with the $NH_3/H_2O_2/H_2O$ sonicating technique. To perform this approach 3 beakers, an ultrasonic cleaner, 10 ml ammonium acid (NH_3), 10 ml hydrogen peroxide 30% (H_2O_2) , 20 ml ultra pure water (H_2O) and parafilm were used.

Firstly, the samples were placed in a beaker containing the solution: $NH_3 : H_2O_2 : H_2O$, 1 : 1 : 2 and then, it was covered using parafilm. Secondly, the glass was placed inside an ultrasonic cleaner and sonicated during 10 minutes. This process had to be carried out three times. Ultimately, the samples were placed in a beaker with H_2O and sonicated in the ultrasonic cleaner for 5 minutes.

The state of the sample (*Phenomen FICH bottom set 17/07*) was observed before and after biofuncionalization, using a confocal bright field optical microscope. Whereas most optomechanical cavities were complete previous to the biofuncionalization (except a few that were broken or presented manufacturing defects), Figure 3.3(a), all of them were broken after biofunctionalization, as shown in Figure 3.3(b). As can be stated from the last figure, this method derived in a dramatic result for the cavities.
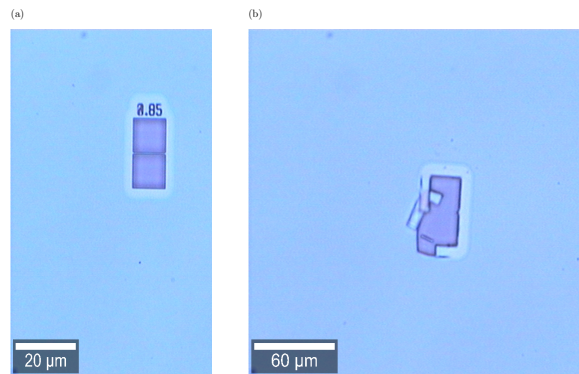

Figure 3.3: Analysis of the state of the cavities under a sonicating technique. (a) State of optomechanical cavities before functionalization. (b) State of optomechanical cavities after functionalization.

Oxygen plasma

As a result of the drawbacks of the sonicating technique for the survival of our devices, an oxygen plasma technique to perform the creation of the -OH groups was addressed. A plasma is an electrically neutral gas consisting of electrons, ions and neutral atoms and molecules in different excited states (its outer electrons do not have to be in the lowest energy state). Oxygen plasma increases the silicon surface hydrophilicity because of increased OH groups (by means of surface oxidation) [34]. According to [35], the process also cleans the surface by removing the impurities and organic contaminants on the surface through chemical reaction with highly reactive oxygen radicals and ablations by energetic oxygen ions.

The oxygen plasma treatment was performed with a Tepla Plasma System, placed at the NTC fabrication laboratories, during 10 minutes at power 400 W, pressure 1.5-1.7 mBar and O_2 flow 100 sccm. This functionalization procedure was tested using a sample containing optomechanical cavities (*Phenomen Fitch Rotated 45⁰*) to verify if they were indeed able to survive this process. As shown in Figure 3.4, all of them were complete previous and after functionalization. Therefore, oxygen plasma was chosen as the technique to prepare our samples for the APTES layer formation. The efficiency of this method will be proved in Chapter 4.1.
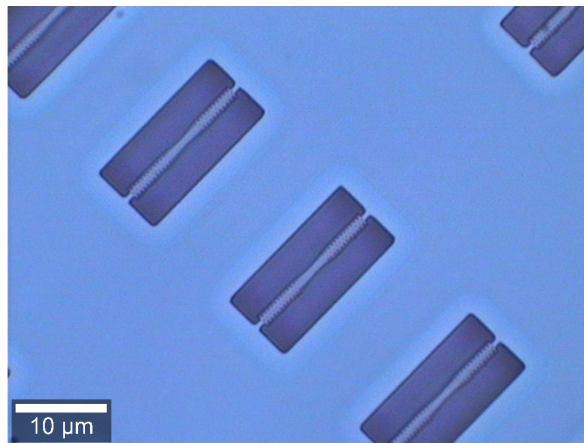
Figure 3.4: Optomechanical cavities after functionalization using oxygen plasma as hydroxylation technique.

3.1.2 APTES monolayer formation

The aim of this second phase is to produce the attachment between APTES and the samples, through silanization [32, 36]. As shown in Figure 3.5, this process involves a condensation reaction thus forming a covalent siloxane linkage (Si-O-Si) as a result [32, 33]. This reaction takes place thanks to the alcoholysis (a type of solvolysis) of APTES, following the chemical Equation 3.1. Absolute ethanol was used as alcohol.

$$R - Si(OET)_3 + R' - OH \rightarrow R - Si(OH)_3 + R' - O - Et \tag{3.1}$$
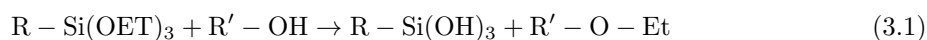
To carry out this technique the materials used were absolute ethanol, a 20 ml sryringe, a 5 ml syringe, APTES, a 0.5-10 μl micropipette, an eppendorf, parafilm, a small beaker and a large beaker. Sulfuric acid (H_2SO_4), hydrogen peroxide (H_2O_2) and ultrapure water were also needed because the beakers

Figure 3.5: APTES functionalized surface as a result of silanization.

were cleaned by means of a piranha solution (H_2SO_4 : H_2O_2 : H_2O, 1 : 1 : 2).

Firstly, absolute ethanol was added to a large beaker. 20 ml were sucked using the 20 ml syringe and introduced to the small beaker. Then, using the 5 ml syringe, 0.2 ml of APTES were sucked and added to the eppendorf. Next, 4,4 μl of APTES were added to the small beaker using the micropipette. The solution was shaken with the tip of the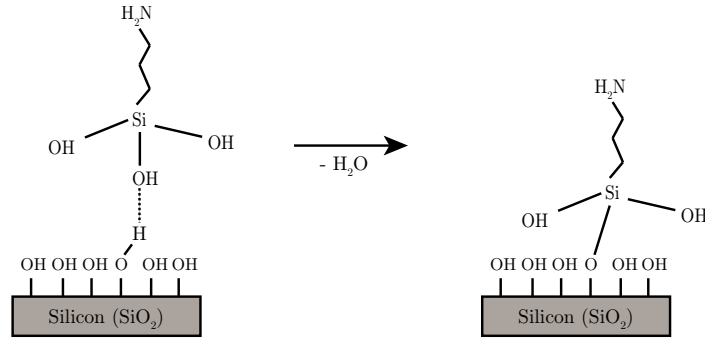 micropipette. The samples were now rinsed with water and blown with nitrogen (N_2). Subsequently they were introduced in the small beaker and it was covered using parafilm. The samples were left in the beaker during 45 minutes. According to [37], this functionalization recipe generates a monolayer of APTES.

3.2 Characterization of optomechanical cavities

3.2.1 Experimental Setup

The OM cavities were characterized through evanescent coupling, because this configuration enables the possibility to manufacture hundreds of cavities without the need of guides in comparison to horizontal and vertical coupling. For instance, this results in a reduction of resources and time from the fabrication point of view. A tapered fiber in a shape of a microloop connected to the tunable infrared laser was used, as this element is capable of coupling light via evanescent waves in and out the cavity. However, in order to ensure coupling between the tapered fiber loop and the cavity, the loop must be placed in a close vecinity. The relative position of the microlooped tapered fiber can be modified using piezo controllers, thus making it possible to position in any specific cavity.

The experimental setup used to acquire the optical and mechanical spectra is sketched in Figure 3.6. The transmission and reflection spectra were characterized through the elements shaded in red and orange in Figure 3.6, respectively. Additionally, the experimental setup is shown in Figure 3.7 and 3.8. As can be appreciated in Figure 3.8, the samples where placed inside a hood in order to take the measurements because the hood stabilizes the measurement process. Under this configuration, the involved elements and their function are:

- Tunable infrared laser: Generates a continuous wave optical signal that will be sent to the device under study. Two different tunable lasers were employed in the experiments. The laser model used to characterize the optical response was Keysight Agilent 8163BB Lightwave Multimeter (λ = 1520-1630 nm) whereas to characterize the mechanical response the model New Focus
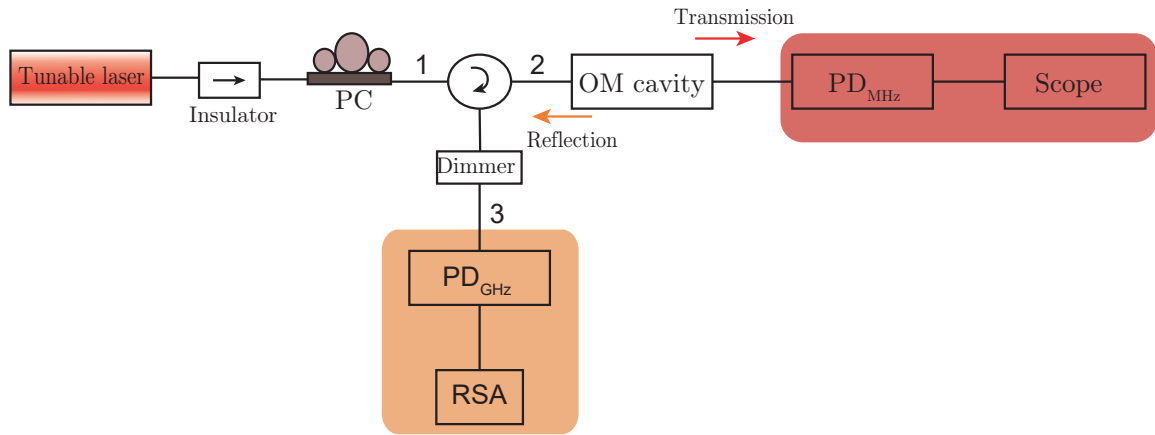
Figure 3.6: Sketch of the experimental setup used to characterize the optomechanical cavities.

TL-6700 (λ = 1520-1570 nm) was employed.

- Polarization controller (PC): Used to select the correct light polarization of the tunable laser to be sent to the cavity in order to transduce the required optical mode. Light, as electromagnetic radiation, is a transverse wave that has both a magnetic and an electric component. In polarized light the vibrations occur in a single plane (Figure 3.9). There are two possible polarities; transverse electric (TE) if the electric field is perpendicular to the plane of incidence and transverse magnetic (TM) if the magnetic field is perpendicular to the plane of incidence. The field designed to be confined in our cavity is TE. Consequently, the laser light has to be TE in order to excite the TE mode. The higher the optical response, the more TE mode is reaching the photodetector. With the PC light polarity can be modified until the response on the photodetector is maximum, thus resulting in a maximum transduction of the required optical mode under study.

- Optical circulator: Light entering through a channel exits through the next channel, thus enabling to collect both the reflected and transmitted signals [23]. The optical spectra was acquired in transmission whilst the mechanical spectra was acquired in reflection.

- Insulator: As the optical circulator can have reflection losses, an insulator is placed to prevent the reflected light from burning the laser by ensuring that light travels in a single direction.

- Photodetector (PD): Light sensor that converts light photons into current. Used to characterize both the optical and mecanical response. In order to characterize the optical response, a MHz PD is applied (New Focus 0901) whereas to characterize the mechanical response a GHz PD is needed (New Focus 1544-B DC-Coupled NIR Fiber-Optic Receiver). Mechanical modes on the order of GHz are of interest because they correspond to mechanical modes confined in the central region of the optomechanical cavities. These will be the mechanical modes that will be used to perform the detection of the deposition of an APTES layer in our experiments.

- Scope: Electronic instrument that graphically represents time-varying electric signals. Included to observe the signal generated by the MHz PD, the transmission spectra. The model used was Agilent DSA80000B High Performance Infiniium Oscilloscope.

- Dimmer: To avoid burning the sensitive GHz PD.
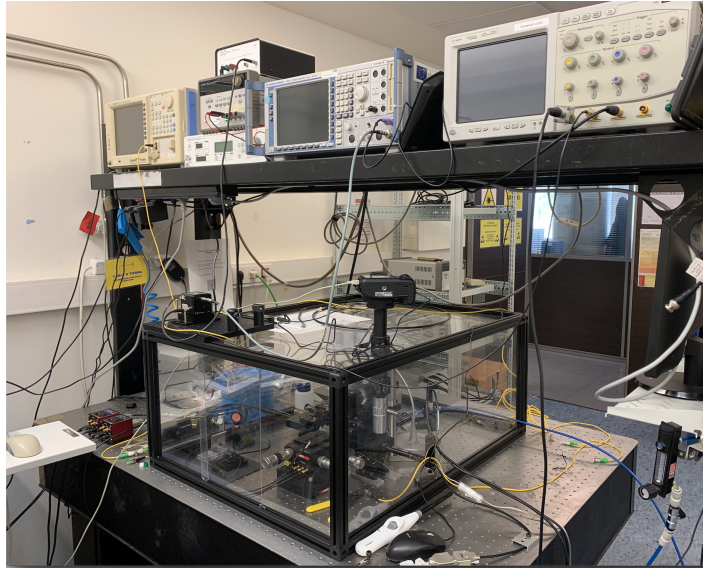
Figure 3.7: General view of the experimental setup used to characterize the optomechanical cavities.
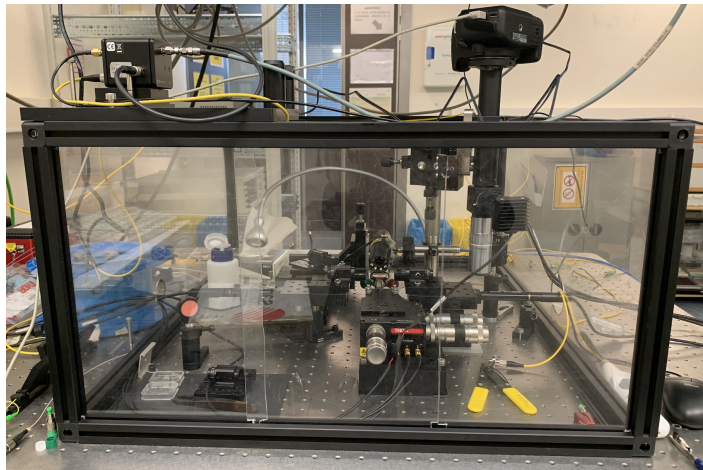
Figure 3.8: View of the hood where the sample was placed in order to take the measurements. Note that the hood stabilizes the measurement process.

- Radiofrequency spectrum analyser (RSA): Electronic device that represents the amplitude of a signal as a function of a selected frequency range. The incoming electrical signal is the signal detected through the GHz PD at the reflection spectra. The model used was Rohde & Schwarz FSQ 40 Signal Analyzer.

In addition to the aforementioned elements, a vertical and a lateral microscope facilitate the visualisation of the cavities and, consequently, the positioning of the microloop.
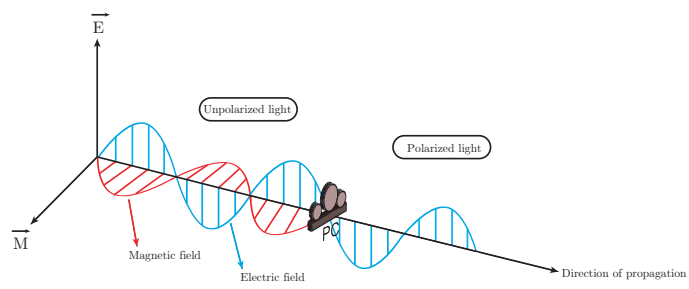
Figure 3.9: Relation between magnetic and electric field in an electromagnetic wave.

Chapter 4

RESULTS

4.1 Verification of effective functionalization

Previous to the analysis of the OM sensor performance under the presence of an APTES layer, a verification of the effectiveness of the functionalization procedure described in Section 3.1 was performed.

4.1.1 Comparative study using negatively charged gold nanoparticles

To verify that it was possible to functionalize effectively the silicon samples and consequently the optomechanical cavities using the aforementioned techniques, a comparative study was carried out. The objective was to analyse surface differences between samples with and whithout APTES by using gold nanoparticles. This is because as gold has chemical affinity for amines, an appreciable difference in the deposition of those particles in that samples should be significant. Otherwise stated, a greater amount of gold nanoparticles are expected to bind to the functionalized surfaces. Furthermore, the gold nanoparticles used were negatively charged. Therefore, protonation of a functionalized sample would further enhance the binding of the gold nanoparticles, because there would exist both chemical and electrostatic attraction.

To this end, 4 silicon samples were used and set under different conditions. As shown in Figure 4.1(a), two of them were functionalized using oxygen plasma and the approach outlined in Section 3.1.2, whilst the other two remained nonfunctionalized. One of the functionalized samples was protonated too, bringing about a cationic surface. Additionally, one of the nonfunctionalized samples was protonated in order to be able to compare with the latter sample. Note that the samples that were not functionalized were cleaned with oxygen plasma before this experiment, so they should exhibit higher hydrophilicity than the functionalized wafers.

To experimentally implement this procedure the materials required were a beaker, parafilm, an orbital stiring, hydrochloric acid (HCl), ultra pure water, water, 59.6 nm gold nanoparticles negatively charged suspended in water, a 20-200 μl micropipette, an eppendorf and a 10 ml syringe and two 5 ml syringes.

Firstly, the samples were introduced in a beaker with ethanol, covered using parafilm and placed in the orbital stiring during 5 minutes. Then, they were placed on a piece of paper and dried under a N_2 stream.

At that point, the HCl was diluted by introducing 9 ml of ultra pure water and 1 ml of HCl in a beaker. The solution was shaken, then the samples that were going to be protonated were added during approximately 7 minutes and covered with parafilm. Next, the samples were rinsed with water and blown with N_2.

By this time the purpose was to add the gold nanoparticles to the samples. 0.5 ml of gold nanoparticles were introduced in an eppendorf using a 5 ml syringe. For the 4 samples the procedure was pipetting 50 μl of nanoparticles using the micropipette and waiting for 1 minute. Next, they were rinsed with water and blown with N_2. As expected, the hydrophobicity of the functionalized samples could be observed, because the entire surface did not get wet. Conversely, the nonfunctionalized samples seemed to be hydrophilic.

To observe the results the samples were analyzed using an atomic force microscope (AFM) in tapping mode. AFM is a type of Scanning Probe Microscopy (SPM), which consists of placing a nano-sized probe very close to the surface to be characterized in such a way that the physical interaction between the probe and the surface can be characterized. In AFM this is an electrostatic force; the probe electrones are repelled by the electrons in the atoms of the surface (Van der Waals forces). Specifically, in tapping mode the probe vibrates on the surface at a certain frequency, having contact with the sample. This mode was used to avoid dragging the gold nanoparticles. As shown in Figure 4.1(b), the functionalized and protonated sample (FP) presented the largest number of gold nanoparticles, followed by the functionalized but not protoned wafer (FNP). Expectedly, the nonfunctionalized samples (NFP, NFNP) didn't present a significant amount of nanoparticles. To count the number of them a programme called flooding was used which counted all the hills taller than a minimum height, which was settled to 15 nm, thus coinciding with the nanoparticles. FP turned out to have 144 nanoparticles, FNP 31, NFP 4 and NFNP 0. As a consequence, effective functionalization could be concluded.

(a)

(b)

Figure 4.1: (a) Scheme of the procedure followed to verify the functionalization of the silicon wafers. (b) AFM results.

4.1.2 Water contact angle measurements

To verify the quality of the functionalization performed to the *Phenomen Fitch Rotated 45⁰* sample, the advancing and receding contact angles were measured using an automatic goniometer (Ramé-Hart Instrument Co., Model 90). According to literature [38] a silicon wafer functionalized with APTES exhibits a contact angle of approximately 59°.

Real, non-ideal surfaces are not completely homogeneous, hence exhibit a range of possible contact angles commonly known as contact angle hysteresis. The largest possible drop that can be originated without expanding the interfacial area between the drop and solid produces a contact angle known as the advancing angle [39]. Likewise, as volume is removed from the drop, the contact angle formed by the smallest volume permissible without the interfacial area diminishing is referred to as the receding angle [39]. The difference between the advancing and receding angle represents the contact angle hysteresis which indicates how rough or chemically heterogeneous the surface is.
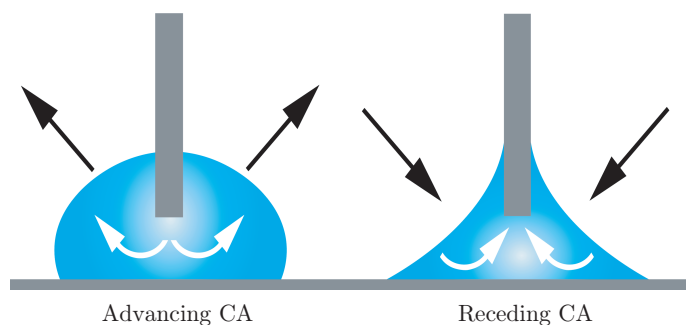

Figure 4.2: Advancing and receding contact angles. Source: Adapted from [40].

The dynamic contact angle technique is also referred to as the add and remove method. 3 rounds of 10 measurements of both adding and removing liquid to the water drop were performed, and measurements of the advancing and receding angles were taken as shown in Figure 4.3. The contact angle was calculated as the mean of the three maximum advancing contact angles. The surface exhibited a contact angle of approximately 67.2° . In addition, an attempt was made to calculate the contact angle of a pretreated silicon surface (with oxygen plasma) but without functionalization (in order to compare them) but the contact angle could not be measured due to drop spreading because of its high hydrophilicity. Effective functionalization could therefore be concluded.

The same procedure was implemented to verify the effectiveness of the APTES layer formation performed to the sample containing the OM cavities characterized before and after functionalization. Figure 4.4 shows how the wafer was indeed effectively functionalized as it exhibited a contact angle of approximately 61.1°.
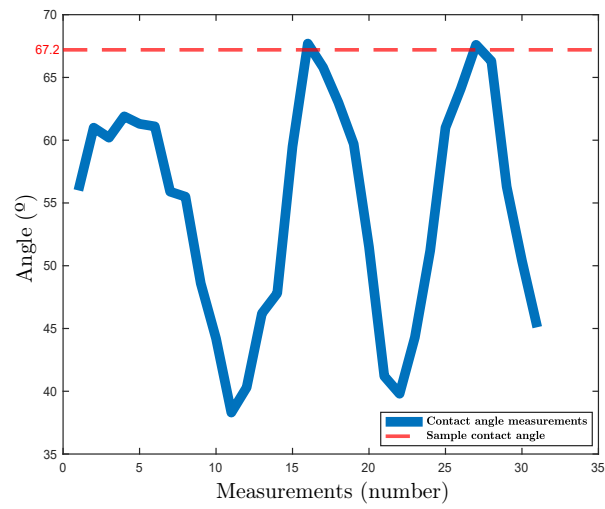
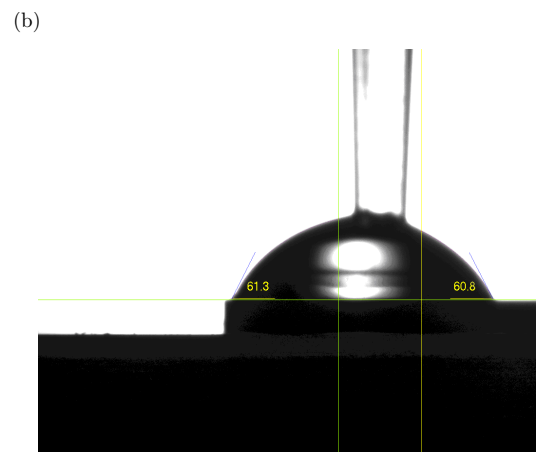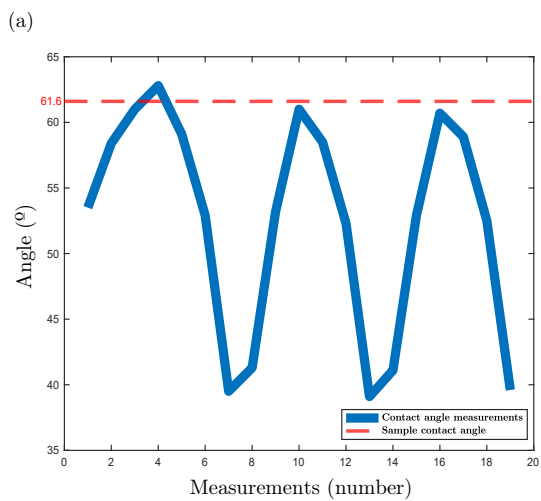Figure 4.3: Dynamic contact angle measurements.

Figure 4.4: (a) Dynamic contact angle measurements. (b) Advancing contact angle.

4.2 Measurements dispersion under different experimental conditions

In order to be able to determine that a possible variation in the optical or mechanical frequency of a cavity when APTES was deposited was due to detection, it was first necessary to characterize the variability of the measurements against different situations to verify that this variation is smaller than that measured by the detection of an APTES layer.

Figure 4.5 shows part of the OM cavities that have been experimentally characterized, and also instantiates how the microloop was positioned at a particular cavity for coupling to occur. Multiple cavities were characterised in case some of them were broken during the functionalization process (the fragility of the cavities must be noted) and because the layer of APTES can be inhomogeneously deposited leading to certain cavities presenting a poorer amount of the molecule.
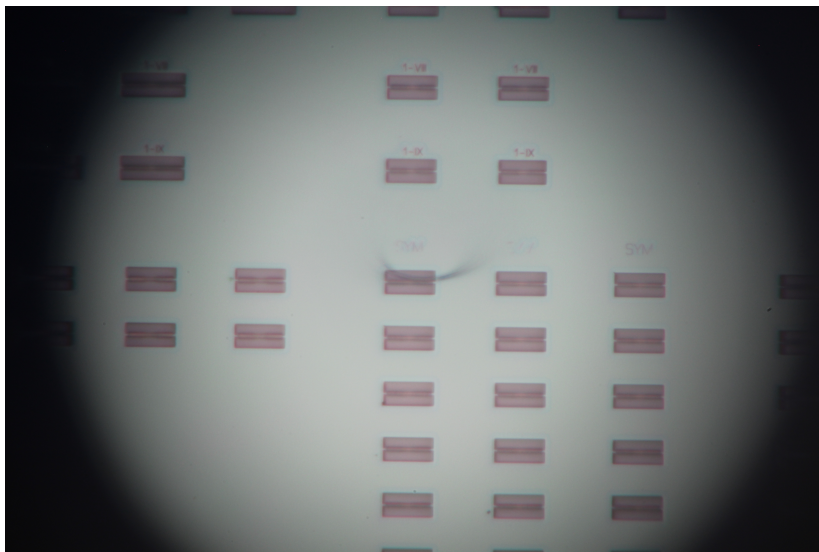
Figure 4.5: View of part of the studied optomechanical cavities.

4.2.1 Optical response variation

During this section optical resonance variations will be characterized, necessary to be able to distinguish between resonance changes produced by the system variability and those due to the presence of APTES. Resonance fluctuations due to different driving power, tapered fiber loop position, polarization and tapered fiber loop were measured. These measurements were performed in the optomechanical cavity coupled with the microloop in Figure 4.5.

All the optical measurements were acquired, as described in Section 3.2, by means of an oscilloscope as a function of time when sweeping the tunable laser across the optical resonance of the cavity. Therefore, in order to correlate the time evolution and the wavelength laser, time units obtained from the scope had to be converted to wavelenght, according to Equation 4.1.

$$\lambda = t \times vl + \lambda l \tag{4.1}$$

where λ is the laser wavelength, t the time, vl the laser velocity and λl the laser initial wavelength. The paremeters vl and λl were programmed to 10 nm/s and 1520 nm, respectively. Figure 4.6(a) depicts an optical response directly obtained from the scope with time units converted to wavelength following the Equation 4.1. In this figure, it can be seen that two superimposed responses can be appreciated: a ripple shape and a peak response. The ripple response corresponds to the behaviour of the tapered fiber loop used to drive power into and out the cavity and the peak response addresses the optical response of the cavity. As we are interested in the optical response of the cavity, a selection of this part of the data will be perfomed and the background noise will be removed.

In order to calculate both the optical quality factor Q_i and the central resonance wavelength a Lorentzian fit was applied to the experimental data. The Lorenztian function is a peak, bell-shaped function given by Equation 4.2, where A is the function's area, x_c and y_c are the central points of the function, and Δ is the FWHM (width at half the maximum value). This parameters are exemplified in Figure 4.6(b). Figure 4.6(c) illustrates the Lorentzian fit calculated to the initial scanning.

$$y = y_0 + (\frac{2 \times A}{\pi}) \times \frac{\Delta}{4 \times ((x - x_c)^2 + \Delta^2)} \tag{4.2}$$

The parameter FWHM can be related to Q_i through the Equation 4.3. Q_i evaluates the goodness of the system as a resonator, as described in Section 2.2. Accordingly, a high quality factor is desired as this implies a narrower resonance and therefore higher detection sensibility.

$$Q = \frac{\lambda}{\Delta \lambda} \tag{4.3}$$
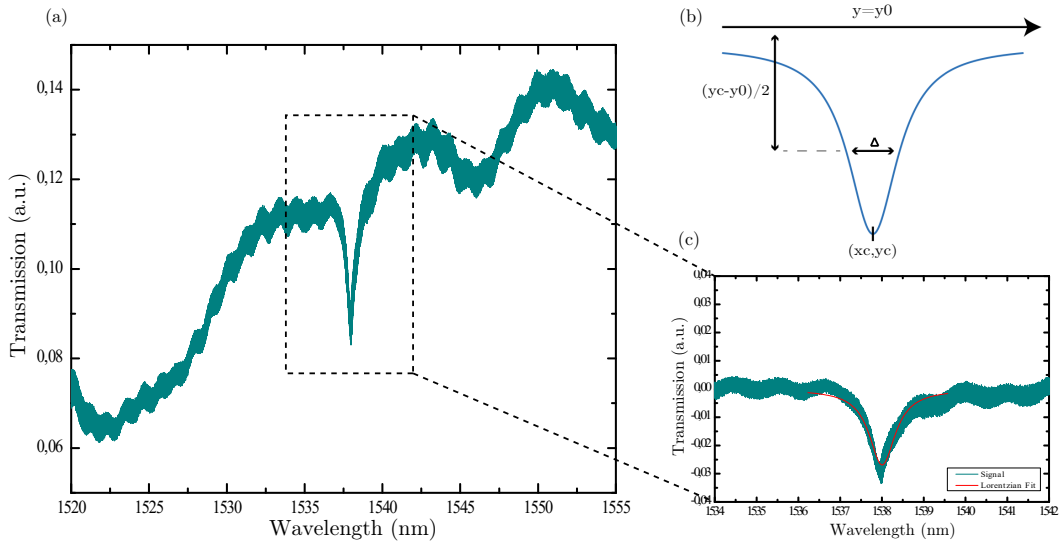
Figure 4.6: (a) Initial scanning before subtracting baseline (b) Lorentz function. (c) Lorentz fit applied to initial scanning.

As previously discussed, in order to ensure that the variability measurements is lower that the frequency shifts resulting from the detection process, different experiments were performed. To begin with, the effect of applying different power to the OM cavities was evaluated. In that respect, at low input powers, the optical response of these cavities had a symmetric shape described by a Lorenztian

shape, as in Figure 4.7(a). However, silicon is a thermo-optical material and is heated up when enough power is applied to it, producing the thermo-optic effect [41]. This effect is more noticeable as power is increased, as revealed in Figure 4.7(b), and can be easily differentiated from a symmetrical response depicted in Figure 4.7(a). The high input power regime will be the working regime that we will employ to transduce the mechanical motion. However, in this section, the optical variability response under different driven conditions will be discussed for low input power. Figure 4.8 represents the wavelength just before coming out of resonance for these cases, and it can be seen that wavelength increases with power.

Note that in Figure 4.6(c) and 4.7(a) both the experimental data (green) and Lorentzian fit (red) are represented. However, in Figure 4.9 and 4.10 only the Lorentzian adjustments are presented.
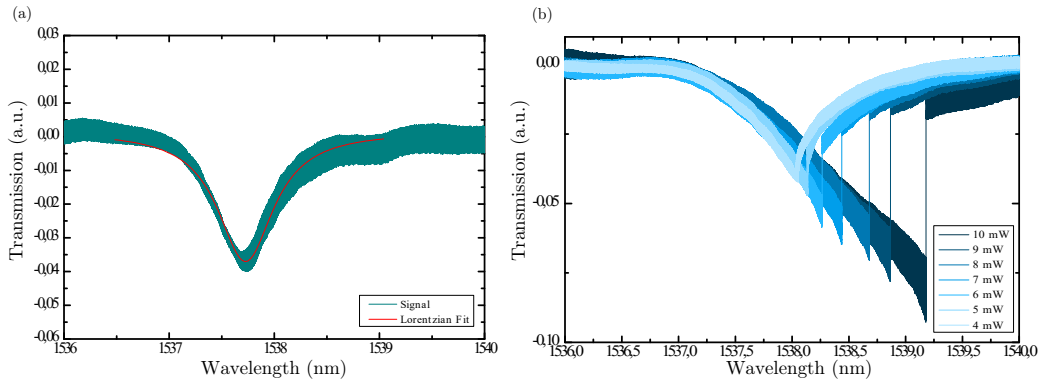
Figure 4.7: (a) An optical resonance depicting a symmetric response. (b) Evolution of thermooptic effect due to increased power.
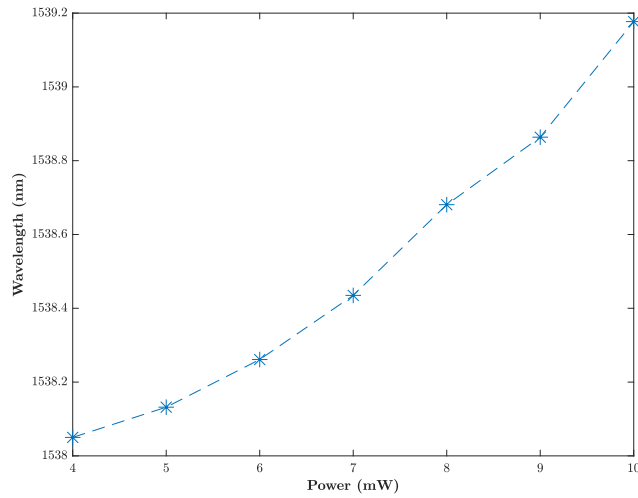
Figure 4.8: Graph showing wavelength before coming out of resonance for different powers

The optical responses measured under different polarization conditions are exposed in Figure 4.9(a), resulting in a optical resonance of $\lambda_r = (1537.84\pm0.07)$ nm. This OM presented a quality factor of $Q_o = 2151\pm140$. Likewise, the optical responses obtained under different fiber-tapered loop positions are shown in Figure 4.9(b). The optical resonance was found to be $\lambda_r = (1537.6\pm0.5)$ nm.

On another side, to assess the effect of different microloops a different OM cavity was used because the previous OM cavity had a deposited particle that made it difficult to continue taking measurements
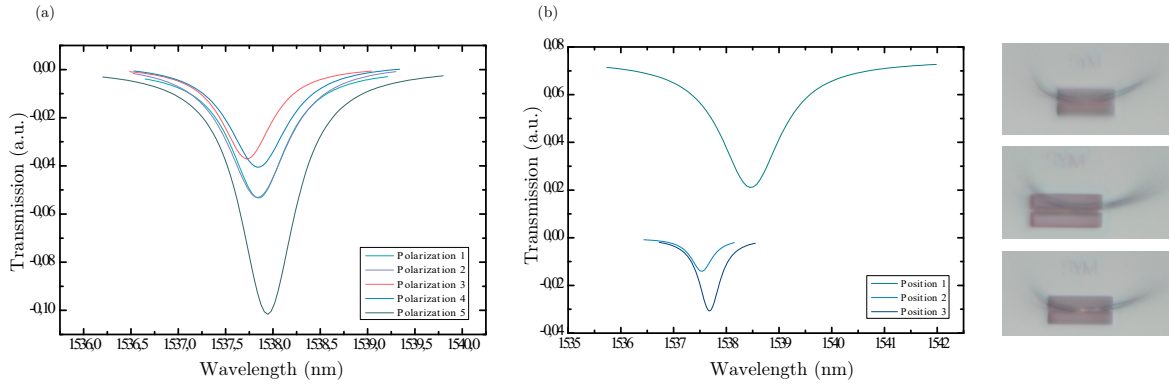
Figure 4.9: (a) Optical resonance for different polarizations. (b) Optical resonance for different loop positions.

on it. Remarkably, fabricating a different microloop also implies the measurements are taken under different polarization, power and position conditions. This study is of relevant importance because different fiber loop tapers were fabricated all along the experiments due to the fact that the fiber loop transmission decays with time. This can be attributed to dust desposition and humidity effects because all the experiments where performed at ambient conditions. Because of that, an analysis of the variability of the measurement with different fiber loops was needed. An optical resonance wavelength of $\lambda_r = (1558.01 \pm 0.14)$ nm was measured as displayed on Figure 4.10. It should be noted that this OM cavity presented an optical quality factor of $Q_o = 3593 \pm 3$.

Table 4.1 sums up the range and standard deviation of the measurements obtained under different experimental conditions.
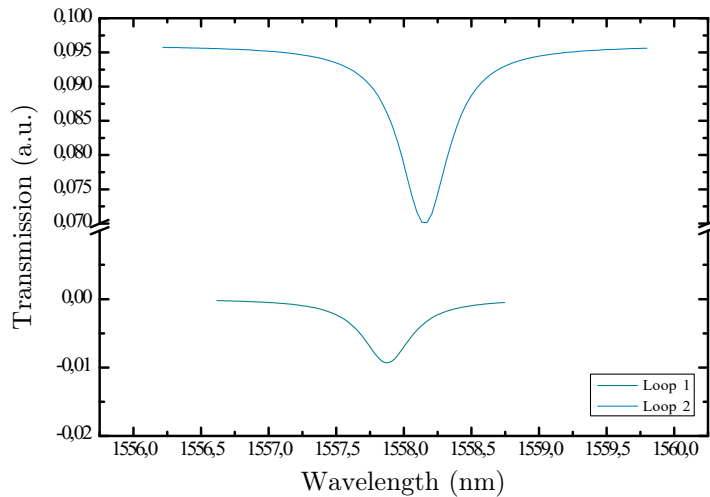
Figure 4.10: Optical resonances measured with different loops.

Table 4.1: Overview of optical resonance variations due to different experimental conditions.

Paramenter changed	Range (nm)	Standard deviation (nm)
Polarization	0.2170	0.07
Position	0.9302	0.50
Loop	0.27835	0.14

4.2.2 Mechanical response variation

In order to characterize the mechanical response of the OM crystal cavities under study, it must be noted that different regimes can be obtained as a function of the laser input power driving the cavity and the optical detuning. This detuning is defined as $\Delta\lambda=\lambda_i\text{-}\lambda_r$, where λ_i is the input laser and λ_r the cavity resonance [5]. Firstly, when driving the cavity with a blue-detuned laser ($\Delta\lambda<0$), the optical wave can efficiently boost the mechanical motion, as can be seen in Figure 4.11(a). This figure shows the experimental mechanical power spectral density obtained from the analysis of the reflection channel via the RF spectrum described in Section 3.2.

However, under high input powers and detunings, an amplification of the mechanical mode occurs and an instability can be attained above the threshold of regenerative oscillation, which results in a very narrow tone in the detected spectrum at the mechanical resonance, known as phonon lasing [1, 22]. This phenomen can be appreciated in Figure 4.12.

Moreover, since OM cavities are nonlinear elements, multiple harmonics of the fundamental mechanical vibrations can be over-imposed on the optical signal, a phenomen interpreted theoretically as an optical frequency comb (OFC) [6]. This OFC can be obtained by means of a high blue-detuned driving as previously said, here, higher-order harmonics can be noticed in the detected signal (shown in Figure 4.11(b)) [6]. It must be noted that going from phonon lasing to the OFC requieres both an increase in the input power and a larger wavelength of the driving laser due to the red-shift of the optical resonance. This phenomen is physically described as an increase in wavelength and is caused by the thermo-optic effect presented in Section 4.2.1 that takes place because of increased power. Lateral panels showing a close view of the first three involved harmonics are shown.

Measurements of higher-order harmonics enhance the systems sensibility because higher frequency shifts are experienced on the higher order harmonics leading to high-resolution mass sensing [1, 16]. Particularly, the induced frequency shift for the corresponding n^{th} harmonic will be n times larger than the frequency shift experienced by the fundamental mechanical mode δf_m, as depicted in Figure 4.11(c) [16].

Nevertheless, it must be noted that in our system different type of mechanical modes can be confined. One of them are the confine mode at the center of the cavity at the GHz regime, as the one depicted in Figure 2.8, but also mechanical displacement corresponding to the vibration of all the suspended cavity can be found at the MHz regime [42]. Figure 4.12 and 4.13 show how the OM cavities also presented mechanical modes on the order of MHz (shaded in green in Figure 4.13), which correspond to the vibrations of the entire cavity [27]. These modes are also noticeable in Figure 4.12. In this work, the mechanical modes on the order of GHz (shaded in pink in Figure 4.13) have been studied, which are due to mechanical fields confined in the cavity central region.

The effect of different microloop positions on the mechanical modes was studied. Figure 4.14 shows the results obtained for two different positions on one same cavity. However, it must be noted that it is very complicated to find two tapered fiber loop positions which efficiently inject power to the cavity in order to generate a stable OFC. In fact, the results depicted in pink in Figure 4.14 show how for that loop position the lasing regime was unstable and, consequently, the third harmonic measurements could not be registered. As a consequence, even though the frequency difference is $\delta f_1 = 9.1$ MHz for the first harmonic and $\delta f_2 = 18.4$ MHz for the second harmonic (these differences are referred to the points with the same power), this results are hardly comparable.
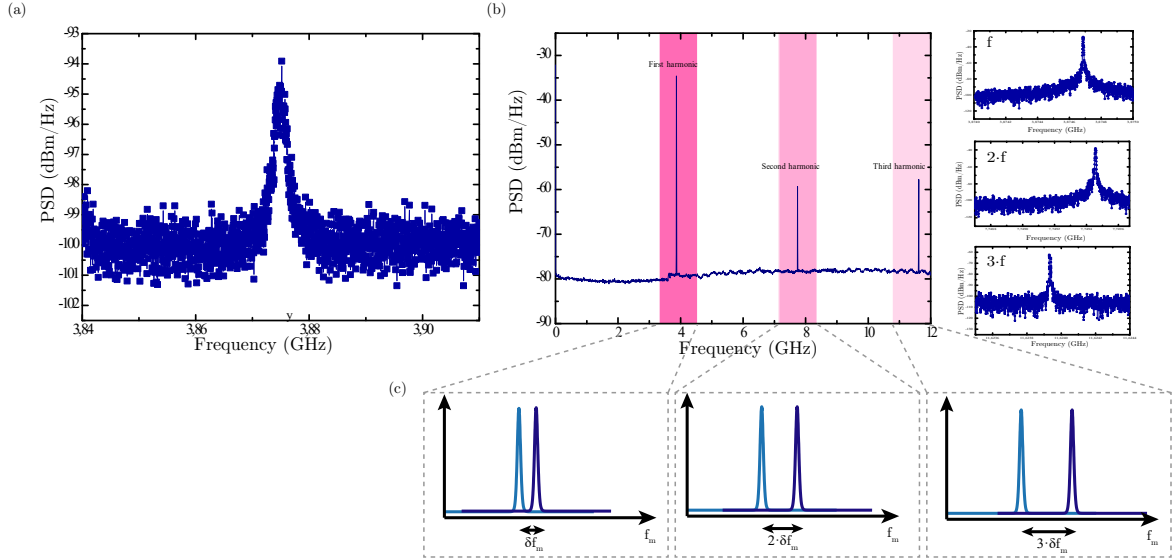
Figure 4.11: (a) Fundamental transduced mechanical mode without phonon lasing. (b) First 3 harmonics under the generation of a OFC and close view of each harmonic. (c) Frequency shifts taking place in the different harmonics under the theoretical presence of a molecule.

The effect of coupling with a different loop was also studied and the results are shown in Figure 4.16. Note that the cavity where these measurements were taken is different from the previous one. It can be appreciated that the driving power of the measurements taken with different loops do not coincide exactly, however, linear extrapolation was applied to the data to make it comparable. The outcomes are a mean frequency shift of $\delta f_1 = 7.82$ MHz, $\delta f_2 = 15.18$ MHz and $\delta f_3 = 22.62$ MHz. It must be highlighted that this measurements correspond to two completely different days and therefore imply different microloop position as well.

To justify why this linear extrapolation is applicable reference will be made to Figure 4.17. The graph shows some measurements taken for different powers, where the fundamental mechanical mode of phonon lasing was measured for the different wavelengths in which the cavity is in resonance. Here, the large number of measurements depict the linear relation between power and frequency. It must be pointed out that in this work all of the measurements were taken at the first wavelength at which the OFC appeared, to ensure that the results are comparable.
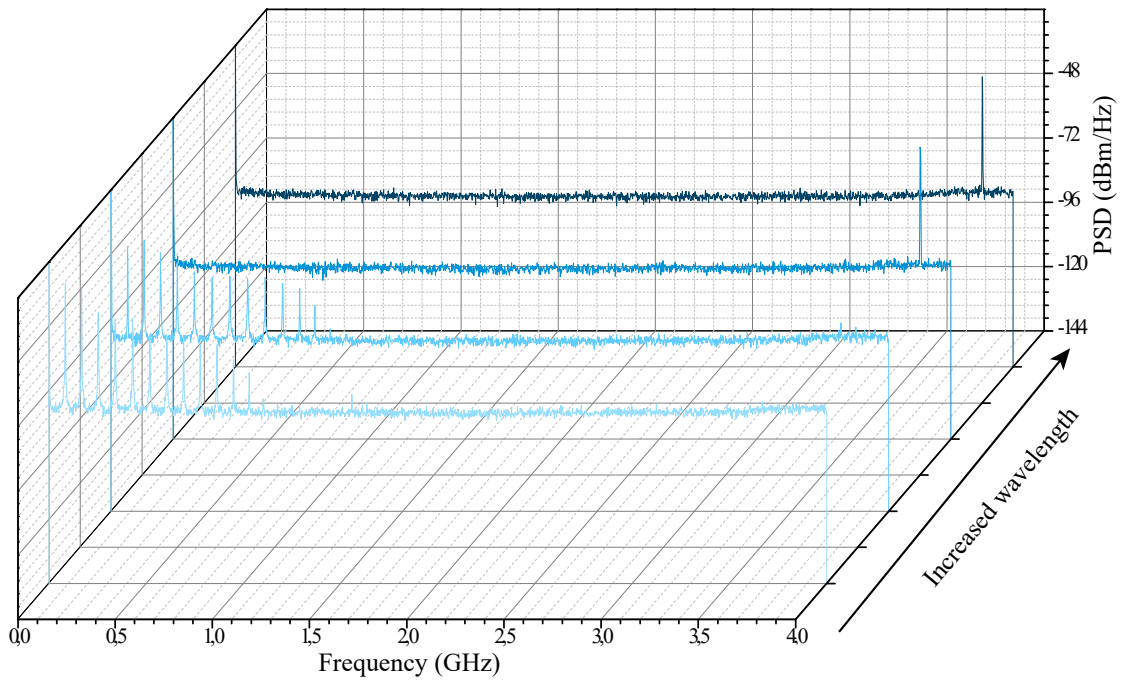
Figure 4.12: Phonon lasing due to blue-detuned driving and high input power.
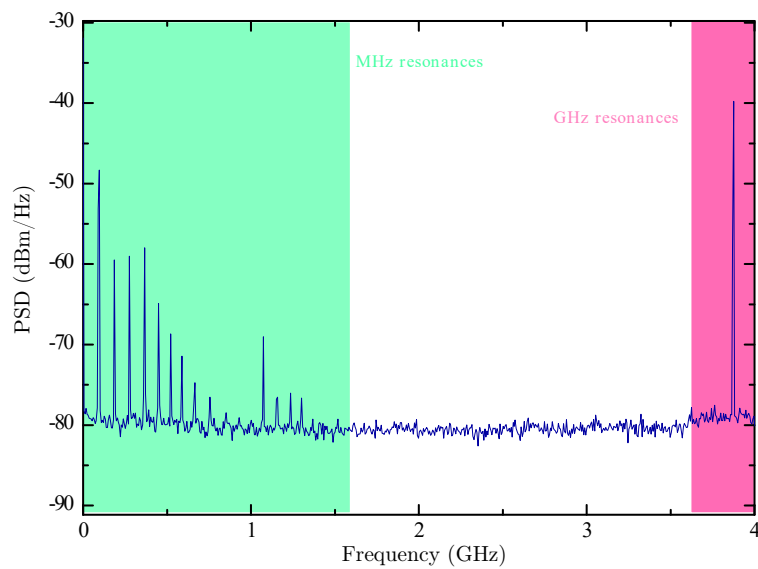
Figure 4.13: Mechanical spectra obtained with the RSA depicting MHz and GHz modes.
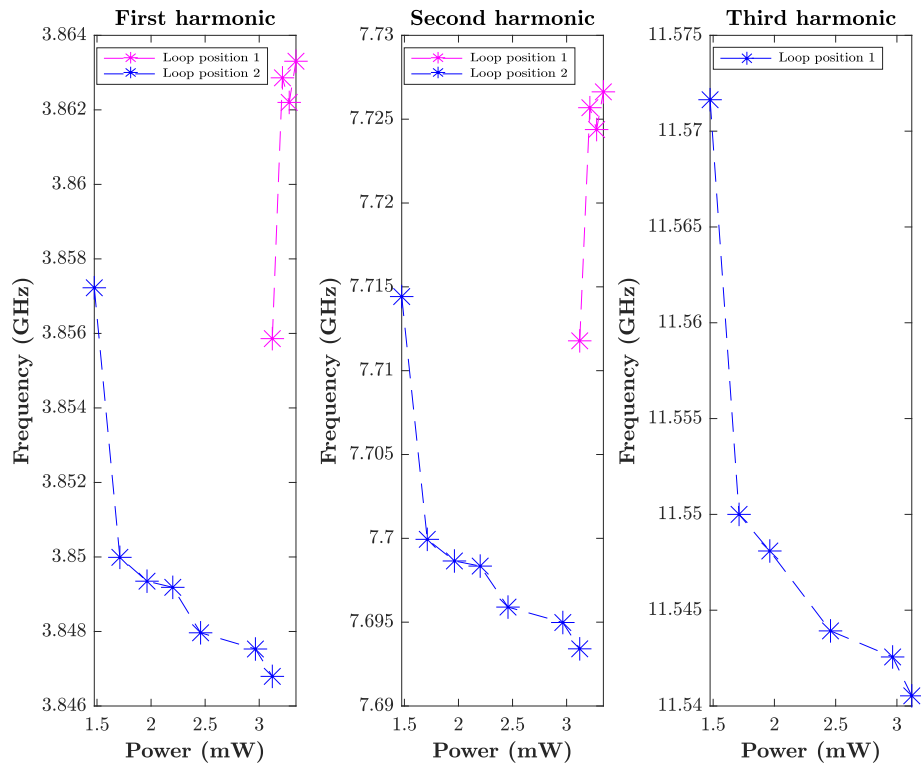
Figure 4.14: Effect of increased power on mechanical response under different loop positions for the first three harmonics of the OFC.
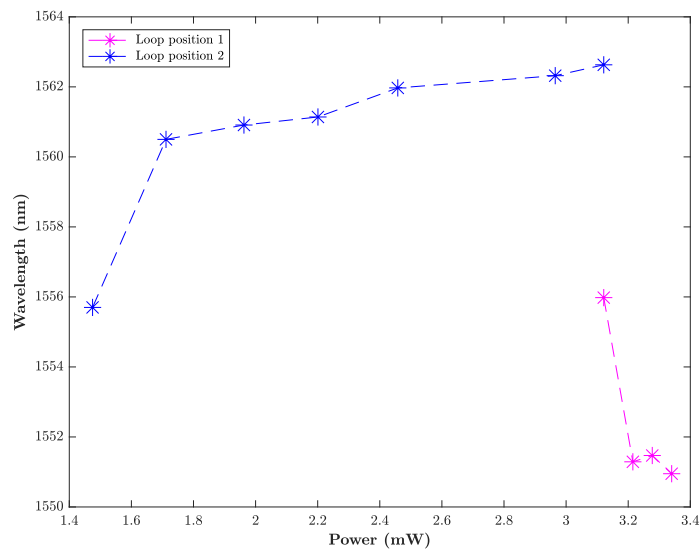
Figure 4.15: Effect of power on wavelength when the mechanical mode is activated in OFC state.
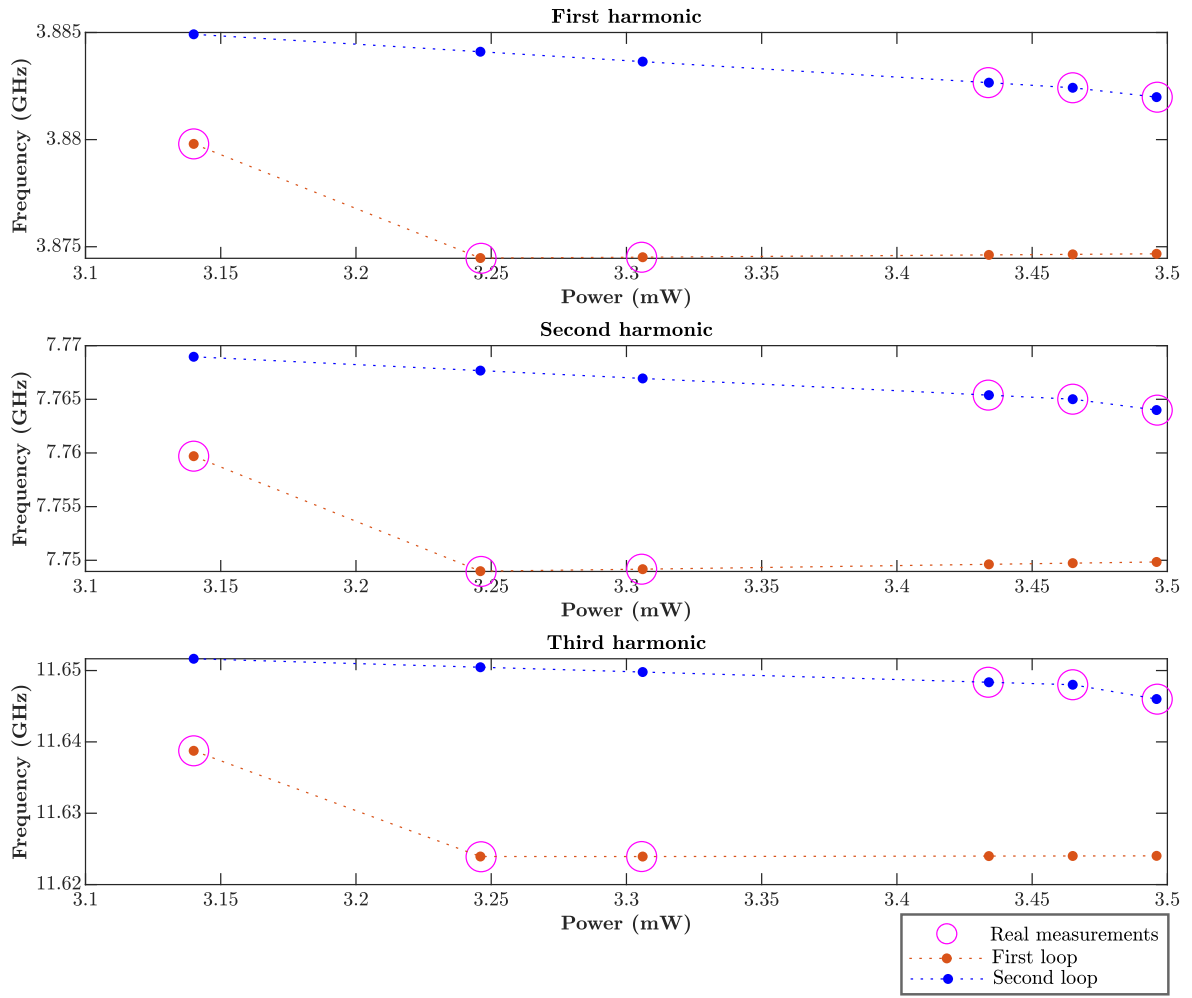
Figure 4.16: Effect of different loop on mechanical response under different loop position and polarization conditions too, for the first three harmonics of the OFC.
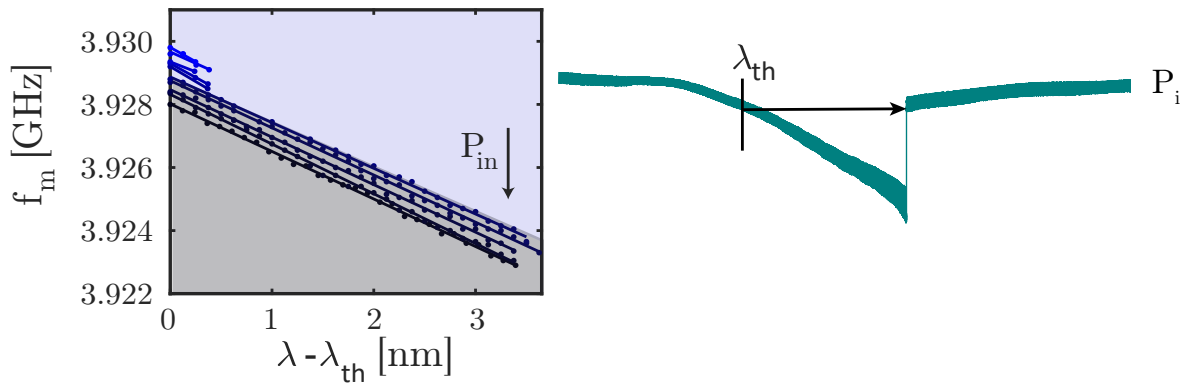
Figure 4.17: Relationship between power, frequency and wavelength.

4.3 APTES detection through the analysis of resonance variations

The deposition of APTES should cause variations optically and mechanically. If the Fabry-Pérot cavity described in Section 2.2 is considered, functionalization would increment the distance between the two mirrors because silicon thickness increases when depositing APTES. Furthermore, the weight of the mirrors is augmented. During this section, the optical and mechanical responses obtained for two different OM cavities before and after functionalization will be described. They will be referred to as *OM cavity 1* and *OM cavity 2*.

Optical resonance

Figure 4.18 and Figure 4.19 show the optical resonance shift experienced by the OM cavities after functionalization with APTES. *OM cavity 1* presented an optical resonance of $\lambda_0 = 1540.4183$ nm before functionalization and of $\lambda_a = 1539.0194$ nm after functionalization, which represents a wavelength shift of $\Delta\lambda = 1.3989$ nm. For *OM cavity 2*, $\lambda_0 = 1539.4615$ nm and $\lambda_a = 1537.7633$ nm, hence undergoing a wavelength shift of $\Delta\lambda = 1.6982$ nm. When compared to Table 4.1, both changes are significantly larger than the variations observed due to our own system variability, and it can therefore be concluded that the presence of APTES can be detected through the optical response.
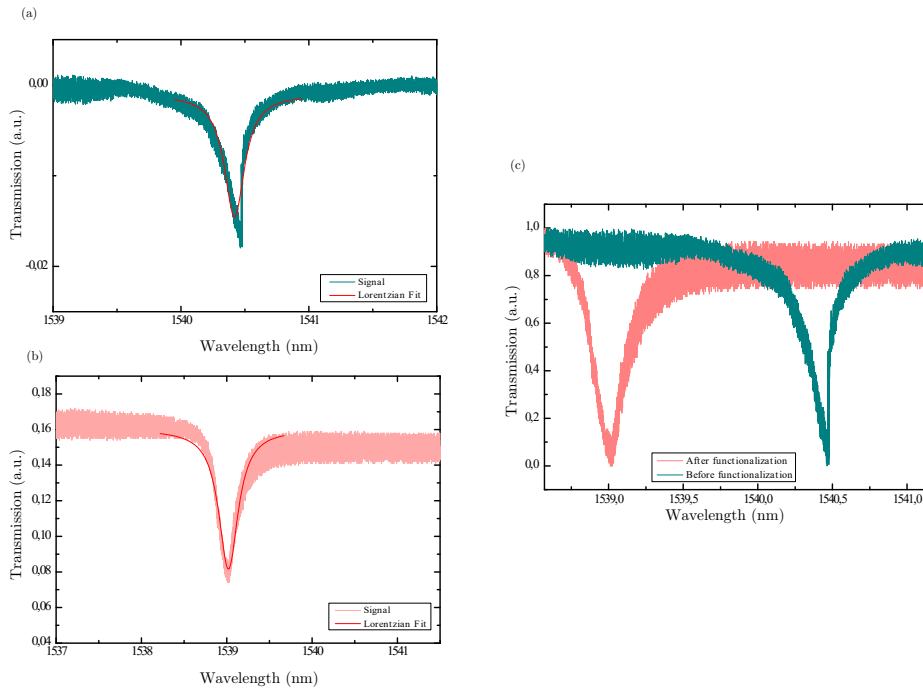
Figure 4.18: *OM cavity 1.* (a) Optical response before functionalization. (b) Optical response after functionalization. (c) Both responses overlapped and standardised.

Mechanical resonance

As mechanical responses could suffer considerably large variations when varying experimental conditions, an experiment where *OM cavity 1* was characterized before and after functionalization on the same day was conducted. Therefore, it was ensured that the fiber tapered microloop, polarization
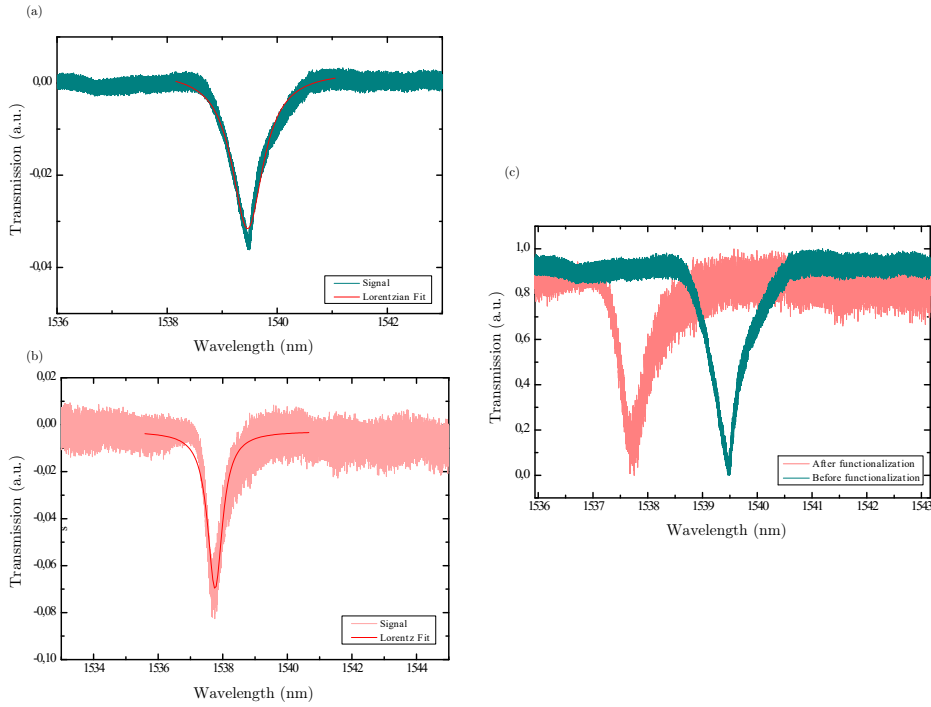
Figure 4.19: *OM cavity 2.* (a) Optical response before functionalization. (b) Optical response after functionalization. (c) Both responses overlapped and standardised.

and power were exactly the same. Moreover, it was assured that the loop position was practically identical, as shown in Figure 4.20.
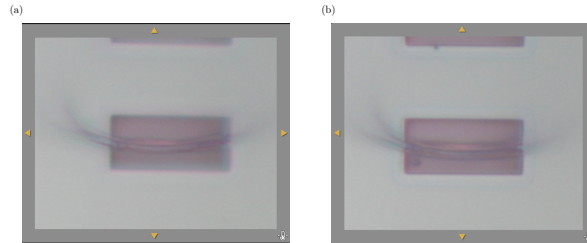

Figure 4.20: *OM cavity 1.*(a) Loop position before functionalization. (c) Loop position after functionalization.

Figure 4.21 displays the frequency shifts measured for different driving powers. The results can be graphically visualized in Figure 4.22. Figure 4.22 represents the mechanical response before functionalization (dark blue) and after functionalization (light blue), for the first three harmonics of the OFC (columns) and increased driving power (rows). The measurements of each peak were taken at high resolution in order to be able to resolve small displacements and acquire the profile of the mechanical resonance at lasing regime accurately. As expected, frequency decreased due to the deposition of APTES because mechanical properties have been changed. The fact that the mass has increased results in mechanical vibrations at a lower frequency. The mean frequency shift is $\delta f_1 = 4.37$ MHz for the first harmonic, $\delta f_2 = 8.03$ MHz for the second harmonic and $\delta f_3 = 11.60$ MHz for the third harmonic. Here, we can see that for higher order harmonics the measured frequency shift is larger, thus resulting in an increment of the sensitivity for higher order frequencies as expected.

For *OM cavity 2* the results were taken on two different days and therefore under different experimental conditions. Here, mechanical response variations due to the systems variability have to be taken into account. However, the measured frequency shifts were far larger, as shown in Figure 4.23. In the
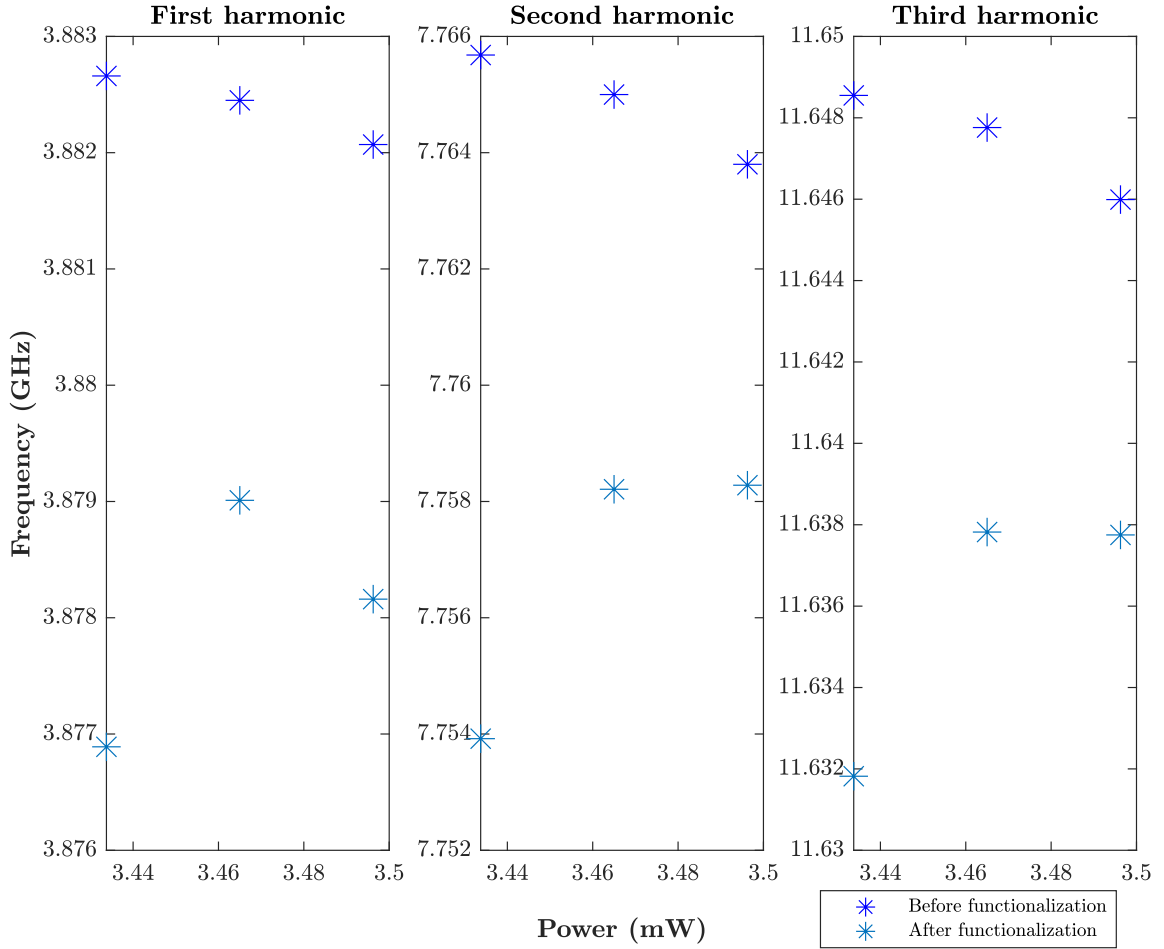
Figure 4.21: *OM cavity 1.* Frequency shifts due to functionalization with APTES for different powers.

latter figure, the responses before (dark blue) and after functionalization (light blue) for the different harmonics are shown together. In addition, on the right there are panels of the amplified responses and the powers at which these resonances were acquired are indicated. It can be appreciated that the power applied to the OM cavity before (3.4587 mW) and after functionalization do not exactly match. Nevertheless, the mechanical resonance after functionalization at a driving power 3.4587 mW can be inferred by linearly interpolating the data between 3.4337 mW and 3.4650 mW. This results in $f_1 = 3.8319$ GHz for the first harmonic, $f_2 = 7.6783$ GHz for the second harmonic and $f_3 = 11.5174$ GHz for the third harmonic. When compared to the mechanical modes before functionalization ($f_1 = 3.8608$ GHz, $f_2 = 7.7210$ GHz and $f_3 = 11.5812$ GHz), the differences obtained are $\delta f_1 = 21.7$ MHz, $\delta f_2 = 42.7$ MHz and $\delta f_3 = 63.8$ MHz. As expected, the sensitivity of the 3rd harmonic is practically three times larger. From that, we can conclude that there was an effective APTES deposition in the sample due to the presence of a high mechanical frequency shift that can not be attributed to the experimental variability.

The frequency changes in this case are much more important, which can be explained because the systems variability is over-imposed to the response and due to an inhomogeneous deposition of APTES. Alternatively stated, as APTES deposition is not completely homogeneous, the results suggest that *OM cavity 2* presented a higher amount of APTES than *OM cavity 1*, thus explaining the different amount of shift measured from the two cavities under study.

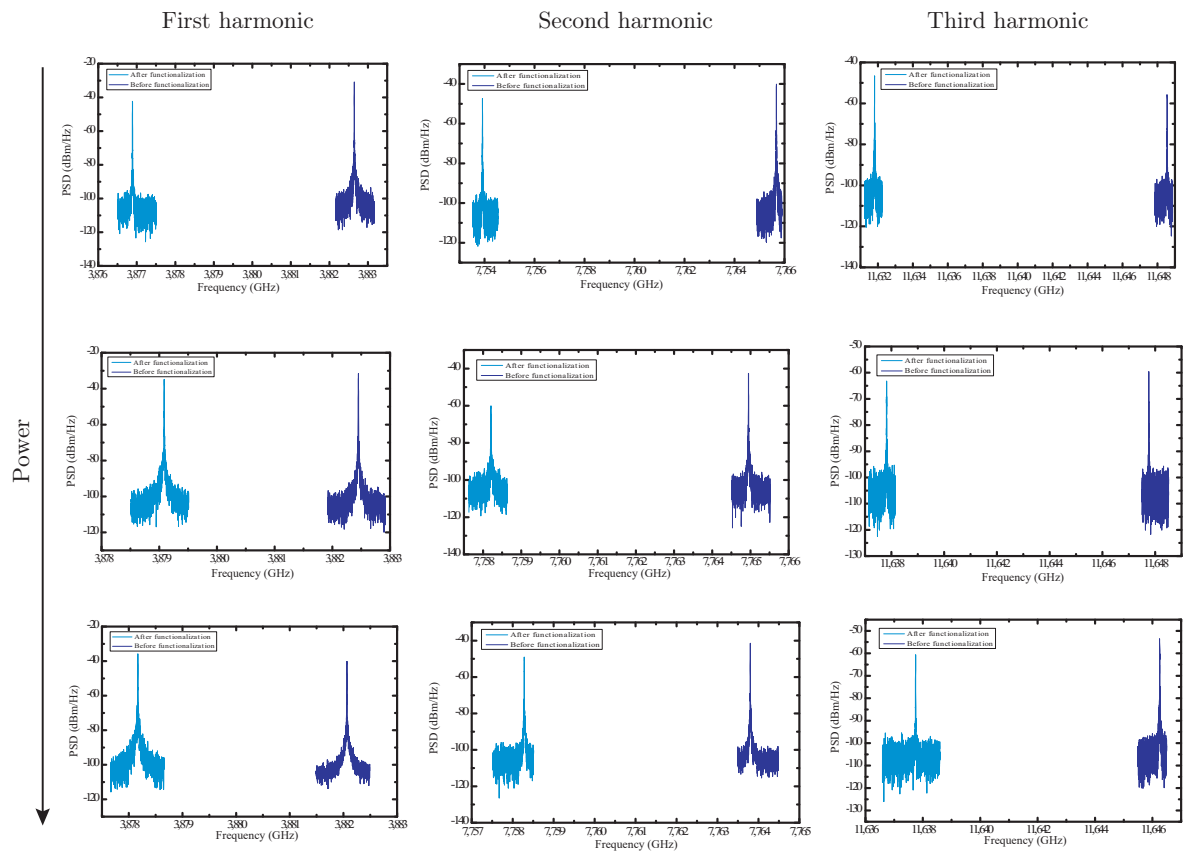Figure 4.22: *OM cavity 1.* Graphical representation of frequency shifts due to functionalization with APTES for different powers.

(a)

(b)

(c)
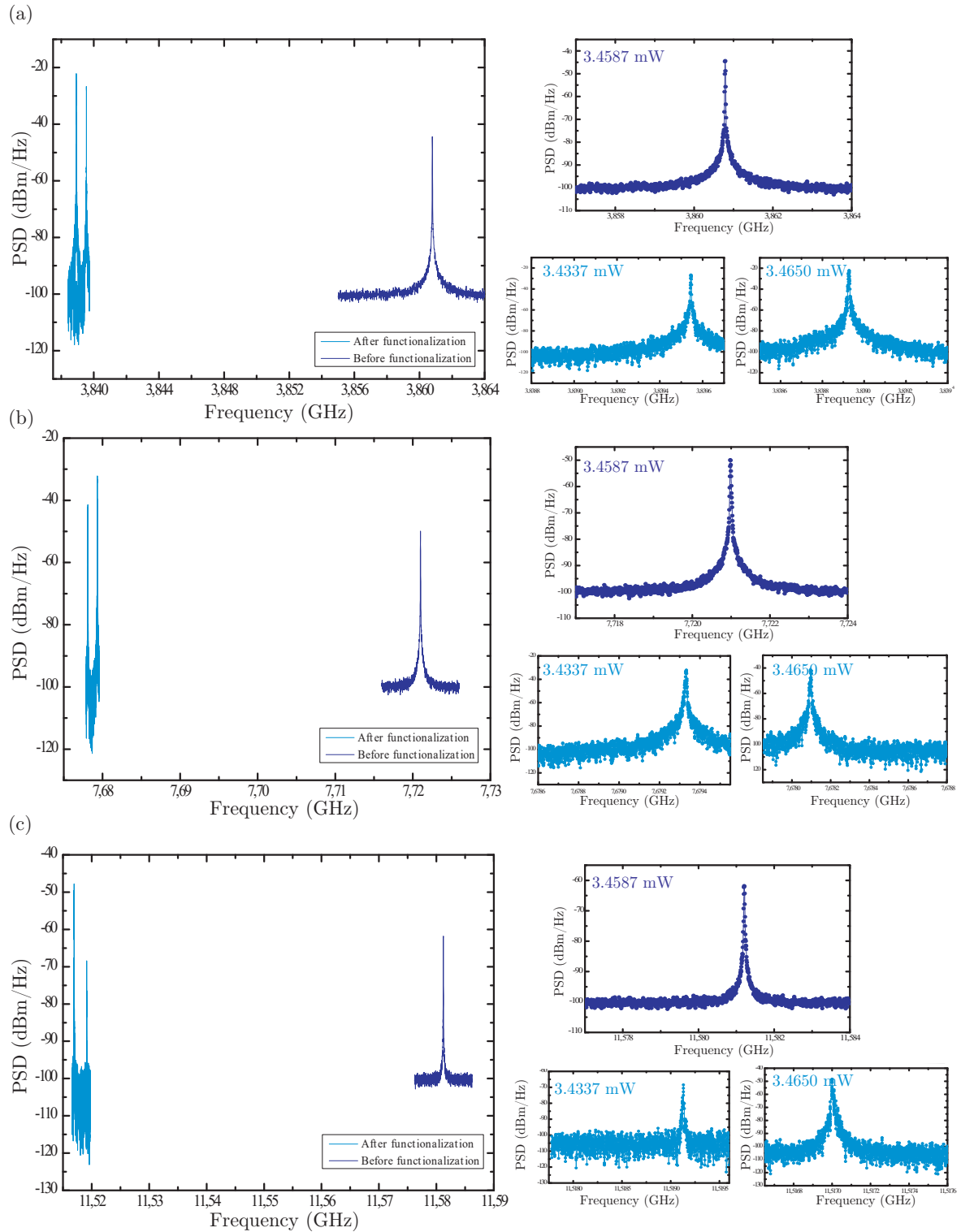
Figure 4.23: *OM cavity 2*. Graphical representation of frequency shifts due to functionalization with APTES.

Chapter 5

CONCLUSION

5.1 Discussion

As discussed in previous sections, the main objetive of this work was to study the performance of OM crystal cavities as dual ultra-sensitive sensors. That means that the purpose was to analyze the capability of the system to detect the presence of an APTES layer.

The results clearly demonstrate that functionalizing with APTES induces significant optical and mechanical resonance variations. Qualitatively, it has been shown that optomechanical crystals are capable of optically and mechanically detecting the presence of a deposited mass. However, the added mass generates a downshift of the mechanical resonance frequency (Δf) that can be transduced to change in mass following Equation 1.1. Accordingly, it is estimated that *OM cavity 1* (where the fundamental mechanical mode experienced a frequency shift of $\delta f_1 = 4.37$ MHz) was covered with $6.06*10^{-19}$ kg of APTES. For *OM cavity 1* (where $\delta f_1 = 21.7$ MHz) a larger amount is estimated, specifically $3.01*10^{-18}$ kg. This results provide a quantitative study of the detection capability of OM crystals. When compared to Table 2.1, the results are definetely state-of-the-art.

Note that the OM crystals presented in this work are $15\mu m * 1\mu m * 220$nm in size, enabling the possibility of integrating hundreds of OM cavities in a single wafer of 6 inches, which in turn permits the performance of multiple lab-on-chip parallel detections. The combination of ultrahigh mechanical eigenfrequencies - beyond gigahertz - together with the low inertial mass and reduced dimensions leads to ultrasensitive biosensing. Additionally, the fact that these oscillators operate at ambient conditions (room temperature and atmospheric pressure) makes these OM crystal nanosensors highly attractive for mainstream health-related applications.

Besides the demonstration of the dual-sensing abilities of the OM cavities, this work provides for the first time evidence of mass sensing of molecular monolayers using this kind of device, which operates at ambient conditions and can be fabricated in standard silicon technology. This finding could lead to the massive deployment of OM cavities as ultra sensitive mass sensors.

5.2 Future work

Although this work only presents the functionality of these optomechanical oscillators as dual sensors of an APTES layer, the fact that the biosensor has satisfactorily been able to optically and mechanically detect the deposition of such monolayer opens the possibility of detecting a target analyte that binds to the functionalized surface in the future. Note that functionalization can be perfomed with another molecule depending on the particular analyte desired to be detected. Given the successful outcomes and the undeniable increasing need of detection of specific biological targets, sensing biochemical entities, particularly variants of COVID-19, is considered the next step to be taken.

To this end, operating the sensor in a fluidic environment is the new perspective to be addressed, given that liquid environments are commonly required for biological applications [4]. According to Gil-Santos et al. [4], the mechanical performance of nanosensors in fluids depends on the resonators dimension, and their study proved that scaling down optomechanical resonators to the nanoscale leads to enhanced achievements. As the OM crystals presented in this work are nanosized, one can expect stunning results when operating in liquid environments. Additionally, high refractive index are required to preserve light-guiding properties [4]. Here, the way of coupling has been by means of a silica fibre, but this has been done as a proof of concept (demonstrate the dual-sensing potential of OM crystals). By introducing the oscillators in an all-silicon integrated system as other authors have done [43, 44] (that is, using another type of coupling such as through a guide), one can take advantage of all the benefits given the high refractive index of silicon. Entirely inmersing these oscillators in fluids would enable both *in situ* and real-time liquid sensing.

The ultimate goal would be to demonstrate if the mass sensitivity of the OM cavities can reach the theoretical limit of 10^{-20} g, which would be a milestone in mass sensing for application in ultrasensitive biological and chemical detection.

Part II

Budget

Chapter 6

Budget

6.1 Introduction

The budget of a project is of relevant significance because it details the financial costs and revenues involved in the project. Microsoft Office (Excel) [45] has been required to calculate the budget of this work. Note that all costs displayed below are approximate and include 21% VAT.

In order to explain what this work entails from an economic point of view, it has been decided to group the activities carried out into 4 fundamental processes: functionalization, characterization of the functionalization, characterization of the optomechanical cavities and data processing and writing. In addition, there is a fifth process which, although not carried out by the participants of this work, is essential for the development of the project: the nanofabrication of the silicon chips containing the optomechanical crystals.

6.2 Detailed budget

This Section provides the detailed budget per process. All of the explanations in this Section refer to Table 6.1. It must be highlighted that all the processes (except nanofabrication) contain an estimate of the cost of staff according to an estimation of the time spent by each member on each process. The hourly rate of the biomedical engineering student has been calculated following Equation 6.1, while the hourly rate of the tutor follows Equation 6.2. In both Equations, SS stands for social security.

$$\frac{20.000\frac{€}{year} + 30\% \, SS}{1800\frac{h}{year}} = 14.4\frac{€}{h} \tag{6.1}$$

$$\frac{40.000\frac{€}{year} + 30\% \, SS}{1800\frac{h}{year}} = 28.88\frac{€}{h} \tag{6.2}$$

The first process considered is functionalization. Here, two types of materials were needed; the so-

called consumable materials (materials physically used up during the experiments) and inventory materials (those that can be reused at the expense of their deterioration). For the latter materials, their unit price has been calculated by dividing their total price by their lifetime, and assuming that they have a lifetime of 100 experiments.

The following process is functionalization characterization, where the different equipment involved in the process can be found. It can be seen that each equipment (found in the laboratories at the Nanophotonics Technology Center) costs 45 euros per hour.

Consecutively, the price of the optomechanical cavity characterization process is exposed, which was carried out by means of the optomechanical setup described in Section 3.2.1 and whose cost was 120 euros per hour. Then, the processing data and writing process is detailed. It can be seen that several softwares were involved in order to fulfill this process.

In order to explain the nanofabrication process costs, it must be firstly taken into account that the chips containing the optomechanical cavities, sized 6 cm^2, are obtained from a wafer whose area is 176 cm^2. Therefore, approximately 30 chips can be obtained from each wafer. It has been decided to calculate the cost per cm^2 of fabricating a wafer (by dividing the total cost of fabricating a wafer by the area) and multiplying by the area of a chip. This assumes that the rest of the wafer will be used to fabricate other chips and will not be wasted.

The general expenses are considered a 12% of the total cost and take into account other indirect expenses (such as utilities and security). Finally, an expected benefit of 6% has been estimated if this project were to be commercialised.

6.3   Summary of the budget by process and by type of cost

Table 6.2 compiles the total cost that each process entails. Additionally, a table summarising the costs according to the type of resources (labour, materials, machinery and others) is inserted to give the reader an idea of which type of resources are the most expensive in this work (Table 6.3). Here, *material* includes both consumable and inventory supplies, *machinery* includes the optomechanical setup and the equipment used for functionalization characterization, *labour* involves the cost of staff for every process and *other* refers to the software licenses required for processing data and writing.

Table 6.1: Detailed budget.

PROCESS / TYPE OF COST	MATERIAL / COST	UNIT	QUANTITY	UNIT COST (euros)	Sub total cost (euros)	TOTAL COST (euros)
FUNCTIONALIZATION						**1.100**
CONSUMABLE MATERIAL: SOLVENTS						
	Ammonium acid	ml	10	0,10	1	
	Ultra pure water	ml	100	0,0013	0,13	
	Hydrochloric acid	ml	1	0,10	0,10	
	Hydrogen peroxide	ml	40	0,11	4,52	
	Sulfuric acid	ml	40	0,11	4,28	
	Gold nanoparticles	ml	0,50	7,75	3,88	
	Absolute ethanol	ml	80	0,02	1,82	
	APTES	ml	0,80	8,90	7,12	
OTHER CONSUMABLE LAB MATERIAL						
	Gloves	u	8	0,27	2,16	
	Syringes	u	10	0,20	2	
	Eppendorf	u	5	0,10	0,50	
INVENTORY MATERIAL						
	Beaker	u	6	0,08	0,48	
	Micropipette	u	2	0,30	0,60	
	Lab coat	u	1	0,15	0,15	
	Fume hood + Nitrogen gas	h	30	2,06	61,80	
COST OF STAFF						
	Biomedical engineering student	h	30	14,40	432	
	Tutor	h	20	28,88	578	
FUNCTIONALIZATION CHARACTERIZATION						**886**
EQUIPMENT						
	Goniometer	h	8	45	360	
	AFM	h	2,00	45	90,00	
	Confocal bright field optical microscope	h	2	45	90	
COST OF STAFF						
	Biomedical engineering student	h	12	14,40	173	
	Tutor	h	6	28,88	173	
OPTOMECHANICAL CAVITIES CHARACTERIZATION						**22.515**
EQUIPMENT						
	Optomechanical setup	h	160	120	19.200	
COST OF STAFF						
	Biomedical engineering student	h	160	14,40	2.304	
	Tutor	h	35	28,88	1.011	
PROCESSING DATA & WRITTING						**3.424**
SOFTWARE LICENSE						
	MATLAB R2019b license (UPV)	u	1	-	-	
	LaTeX	u	1	-	-	
	Microsoft Office license (UPV)	u	1	-	-	
	Adobe ilustrator	month	3	36	109	
	OriginLab	year	1	58	58	
COST OF STAFF						
	Biomedical engineering student	h	148	14,40	2.131	
	Tutor	h	39	28,88	1.126	
NANOFABRICATION						**153**
CONSUMABLE MATERIALS						
	6''SOI wafer	cm2	6	1,42	8,52	

Resin and resing coating, curing and developing processes	cm2	6	0,85	5,11	
Electron beam lithography	h	8	17,05	136,36	
ICP-RIE etching	cm2	6	0,51	3,07	

TOTAL COST	**28.078**
GENERAL EXPENSES (12 %)	**3.369**
TOTAL COST AFTER GENERAL EXPENSES	**31.447**
INDUSTRIAL PROFIT (6 %)	**1.887**
TOTAL CONTRACT ESTIMATE	**33.334**

Table 6.2: Budget by process.

BUDGET BY PROCESS	TOTAL COST (euros)
FUNCTIONALIZATION	1.100
FUNCTIONALIZATION CHARACTERIZATION	886
OPTOMECHANICAL SETUP	22.515
NANOFABRICATION	153
PROCESSING DATA & WRITTING	3.424
TOTAL COST	28.078
GENERAL EXPENSES (12 %)	3.369
TOTAL COST AFTER GENERAL EXPENSES	31.447
INDUSTRIAL PROFIT (6%)	1.887
TOTAL CONTRACT ESTIMATE	33.334

Table 6.3: Budget by type of cost.

BUDGET BY TYPE OF COST	TOTAL COST (euros)
MATERIAL	244
MACHINERY	19.740
LABOUR	7.927
OTHER	167
TOTAL COST	28.078
GENERAL EXPENSES (12 %)	3.369
TOTAL COST AFTER GENERAL EXPENSES	31.447
INDUSTRIAL PROFIT (6%)	1.887
TOTAL CONTRACT ESTIMATE	33.334

Bibliography

[1] W. Yu, W. C. Jiang, Q. Lin, and T. Lu, "Cavity optomechanical spring sensing of single molecules.," *Nature communications*, vol. 7, p. 12311, Jul 2016.

[2] J. Tamayo, P. Kosaka, J. Ruz, A. Paulo, and M. Calleja, "Biosensors based on nanomechanical systems," *Chemical Society reviews*, vol. 42, 11 2012.

[3] D. Akin and R. Bashir, "Single virus particle detection using microresonators with nanoscale thickness," *Applied Physics Letters - APPL PHYS LETT*, vol. 84, 03 2004.

[4] E. Gil-Santos, C. Baker, D. T. Nguyen, W. Hease, C. Gomez, A. Lemaître, S. Ducci, G. Leo, and I. Favero, "High-frequency nano-optomechanical disk resonators in liquids," *Nature Nanotechnology*, vol. 10, no. 9, pp. 810–816, 2015.

[5] F. Pan, K. Cui, G. Bai, X. Feng, F. Liu, and W. Zhang, "Radiation-pressure-antidamping enhanced optomechanical spring sensing," *ACS Photonics*, vol. 5, 09 2018.

[6] L. Mercadé, L. L. Martín, A. Griol, D. Navarro-Urrios, and A. Martínez, "Microwave oscillator and frequency comb in a silicon optomechanical cavity with a full phononic bandgap," *Nanophotonics*, vol. 9, no. 11, pp. 3535–3544, 2020.

[7] M. S. Hanay, S. Kelber, A. K. Naik, D. Chi, S. Hentz, E. C. Bullard, E. Colinet, L. Duraffourg, and M. L. Roukes, "Single-protein nanomechanical mass spectrometry in real time," *Nature Nanotechnology*, vol. 7, no. 9, pp. 602–608, 2012.

[8] K. Jensen, K. Kim, and A. Zettl, "An atomic-resolution nanomechanical mass sensor," *Nature Nanotechnology*, vol. 3, no. 9, pp. 533–537, 2008.

[9] L. Mercadé, K. Pelka, R. Burgwal, A. Xuereb, A. Martínez, and E. Verhagen, "Floquet phonon lasing in multimode optomechanical systems," 2021.

[10] Y. M. Bar-On, A. Flamholz, R. Phillips, and R. Milo, "Sars-cov-2 (covid-19) by the numbers.," *eLife*, vol. 9, Apr 2020.

[11] "https://www.originlab.com," 2021.

[12] "https://matlabacademy.mathworks.com/es," 2021.

[13] R. Karlsson, "Spr for molecular interaction analysis: A review of emerging application areas," *Journal of molecular recognition : JMR*, vol. 17, pp. 151–61, 05 2004.

[14] F. Vollmer, D. Braun, A. Libchaber, M. Khoshsima, I. Teraoka, and S. Arnold, "Protein detection by optical shift of a resonant microcavity," *Applied Physics Letters*, vol. 80, p. 4057, 04 2002.

[15] S. Mandal and D. Erickson, "Nanoscale optofluidic sensor arrays," *Opt. Express*, vol. 16, pp. 1623–1631, Feb 2008.

[16] F. Liu, S. Alaie, Z. C. Leseman, and M. Hossein-Zadeh, "Sub-pg mass sensing and measurement with an optomechanical oscillator," *Opt. Express*, vol. 21, pp. 19555–19567, Aug 2013.

[17] J. L. Arlett, E. B. Myers, and M. L. Roukes, "Comparative advantages of mechanical biosensors," *Nature Nanotechnology*, vol. 6, no. 4, pp. 203–215, 2011.

[18] J. Fritz, M. K. Baller, H. P. Lang, H. Rothuizen, P. Vettiger, E. Meyer, H. Güntherodt, C. Gerber, and J. K. Gimzewski, "Translating biomolecular recognition into nanomechanics.," *Science (New York, N.Y.)*, vol. 288, pp. 316–8, Apr 2000.

[19] J. Chaste, A. Eichler, J. Moser, G. Ceballos, R. Rurali, and A. Bachtold, "A nanomechanical mass sensor with yoctogram resolution," *Nature Nanotechnology*, vol. 7, no. 5, pp. 301–304, 2012.

[20] T. P. Burg, M. Godin, S. M. Knudsen, W. Shen, G. Carlson, J. S. Foster, K. Babcock, and S. R. Manalis, "Weighing of biomolecules, single cells and single nanoparticles in fluid," *Nature*, vol. 446, no. 7139, pp. 1066–1069, 2007.

[21] K. J. V. T. J. Kippenberg, "Cavity optomechanics: Back-action at the mesoscale," *American Association for the Advancement of Science*, 2008.

[22] M. Aspelmeyer, T. J. Kippenberg, and F. Marquardt, "Cavity optomechanics," *Reviews of Modern Physics*, vol. 86, p. 1391–1452, Dec 2014.

[23] D. Navarro-Urrios, E. Kang, P. Xiao, M. F. Colombano, G. Arregui, B. Graczykowski, N. E. Capuj, M. Sledzinska, C. M. Sotomayor-Torres, and G. Fytas, "Optomechanical crystals for spatial sensing of submicron sized particles," *Scientific Reports*, vol. 11, no. 1, p. 7829, 2021.

[24] M. Eichenfield, J. Chan, R. M. Camacho, K. J. Vahala, and O. Painter, "Optomechanical crystals.," *Nature*, vol. 462, pp. 78–82, Nov 2009.

[25] M. Oudich, S. El-Jallal, Y. Pennec, B. Djafari-Rouhani, J. Gomis-Bresco, D. Navarro-Urrios, C. Sotomayor Torres, A. Martínez, and A. Makhoute, "Optomechanic interaction in a corrugated phoxonic nanobeam cavity," *Physical Review B*, vol. 89, 06 2014.

[26] Y. Pennec, V. Laude, N. Papanikolaou, B. Djafari-Rouhani, M. Oudich, S. E. Jallal, J. C. Beugnot, J. M. Escalante, and A. Martínez, "Modeling light-sound interaction in nanoscale cavities and waveguides," *Nanophotonics*, vol. 3, no. 6, pp. 413–440, 2014.

[27] A. C. Montoro, "Excitación de cavidades optomecánicas mediante acopladores "grating" para procesado fotónico de señales de microondas," Master's thesis, Universitat Politècnica de València, 2020.

[28] X. M. Henry Huang, C. A. Zorman, M. Mehregany, and M. L. Roukes, "Nanodevice motion at microwave frequencies," *Nature*, vol. 421, no. 6922, pp. 496–496, 2003.

[29] E. Gil-Santos, J. J. Ruz, O. Malvar, I. Favero, A. Lemaître, P. M. Kosaka, S. García-López, M. Calleja, and J. Tamayo, "Optomechanical detection of vibration modes of a single bacterium," *Nature Nanotechnology*, vol. 15, no. 6, pp. 469–474, 2020.

[30] J. Burkhartsmeyer, Y. Wang, K. S. Wong, and R. Gordon, "Optical trapping, sizing, and probing acoustic modes of a small virus," *Applied Sciences*, vol. 10, no. 1, 2020.

[31] B. Arkles, A. Maddox, M. Singh, J. Zazyczny, and J. Matisons, *Silane Coupling Agents*. Gelest, Inc., 2014.

[32] R. G. Acres, A. V. Ellis, J. Alvino, C. E. Lenahan, D. A. Khodakov, G. F. Metha, and G. G. Andersson, "Molecular structure of 3-aminopropyltriethoxysilane layers formed on silanol-terminated silicon surfaces," *J. Phys. Chem. C*, vol. 116, pp. 6289–6297, Mar. 2012.

[33] J. A. Howarter and J. P. Youngblood, "Optimization of silica silanization by 3-aminopropyltriethoxysilane," *Langmuir*, vol. 22, pp. 11142–11147, Dec. 2006.

[34] A. U. Alam, M. Howlader, and M. Deen, "The effects of oxygen plasma and humidity on surface roughness, water contact angle and hardness of silicon, silicon dioxide and glass," *Journal of Micromechanics and Microengineering*, vol. 24, p. 035010, 02 2014.

[35] N. S. K. Gunda, M. Singh, L. Norman, K. Kaur, and S. K. Mitra, "Optimization and characterization of biomolecule immobilization on silicon substrates using (3-aminopropyl)triethoxysilane (aptes) and glutaraldehyde linker," *Applied Surface Science*, vol. 305, pp. 522–530, 2014.

[36] M. Terracciano, I. Rea, J. Politi, and L. D. Stefano, "Optical characterization of aminosilane-modified silicon dioxide surface for biosensing," *Journal of the European Optical Society - Rapid publications*, vol. 8, no. 0, 2013.

[37] E. Coronado, A. Forment-Aliaga, E. Pinilla-Cienfuegos, S. Tatay, L. Catala, and J. A. Plaza, "Nanopatterning of anionic nanoparticles based on magnetic prussian-blue analogues," *Advanced Functional Materials*, vol. 22, no. 17, pp. 3625–3633, 2012.

[38] X.-C. Lo, J.-Y. Li, M.-T. Lee, and D.-J. Yao, "Frequency shift of a sh-saw biosensor with glutaraldehyde and 3-aminopropyltriethoxysilane functionalized films for detection of epidermal growth factor," *Biosensors*, vol. 10, p. 92, 08 2020.

[39] C. Clegg, *Contact Angle Made Easy.* Carl Clegg, 2019.

[40] "https://www.biolinscientific.com/measurements/dynamic-contact-angle."

[41] D. Navarro-Urrios, J. Gomis-Bresco, S. El-Jallal, M. Oudich, A. Pitanti, N. Capuj, A. Tredicucci, F. Alzina, A. Griol, Y. Pennec, B. Djafari-Rouhani, A. Martínez, and C. M. Sotomayor Torres, "Dynamical back-action at 5.5 ghz in a corrugated optomechanical beam," *AIP Advances*, vol. 4, no. 12, p. 124601, 2014.

[42] J. Gomis-Bresco, D. Navarro-Urrios, M. Oudich, S. El-Jallal, A. Griol, D. Puerto, E. Chavez, Y. Pennec, B. Djafari-Rouhani, F. Alzina, A. Martínez, and C. M. S. Torres, "A one-dimensional optomechanical crystal with a complete phononic band gap," *Nature Communications*, vol. 5, p. 4452, July 2014.

[43] H. Ren, M. H. Matheny, G. S. MacCabe, J. Luo, H. Pfeifer, M. Mirhosseini, and O. Painter, "Two-dimensional optomechanical crystal cavity with high quantum cooperativity," *Nature Communications*, vol. 11, no. 1, p. 3373, 2020.

[44] G. S. MacCabe, H. Ren, J. Luo, J. D. Cohen, H. Zhou, A. Sipahigil, M. Mirhosseini, and O. Painter, "Nano-acoustic resonator with ultralong phonon lifetime.," *Science (New York, N.Y.)*, vol. 370, pp. 840–843, Nov 2020.

[45] "https://www.microsoft.com/es-es/microsoft-365/excel."